RESEARCH ARTICLE

Key Points:
- Rocks in the Sutlej area of the NW Himalaya record Barrovian metamorphism
- Partial meting and decompression occurred during the Miocene
- The Leo Pargil dome was exhumed during orogen-parallel extension

Supporting Information:
- Captions for Tables S1–S4
- Table S1
- Table S2
- Table S3
- Table S4

Correspondence to:
M. J. Jessup,
mjessup@utk.edu

Crustal thickening, Barrovian metamorphism, and exhumation of midcrustal rocks during doming and extrusion: Insights from the Himalaya, NW India

M. J. Jessup[1], J. M. Langille[2], J. M. Cottle[3], and T. Ahmad[4]

[1]Department of Earth and Planetary Sciences, University of Tennessee, Knoxville, Knoxville, Tennessee, USA, [2]Department of Environmental Studies, University of North Carolina at Asheville, Asheville, North Carolina, USA, [3]Department of Earth Science, University of California, Santa Barbara, California, USA, [4]Department of Geology, University of Delhi, Delhi, India

Abstract Rocks exposed in NW India constrain the burial, partial melting, and exhumation history of the Himalayan crust. New microscale and mesoscale structural analysis, combined with pressure-temperature estimates from the Haimanta Group exposed in the Sutlej Valley, indicate that the rocks were folded by two generations of NW trending folds. Barrovian metamorphism culminated at ~30 Ma with staurolite and kyanite overgrowths of F2 folds. Crustal thickening created a metamorphic field gradient that increases from the garnet zone (499 ± 99°C and 4.5 ± 1.4 kbar to 571 ± 92°C and 7.8 ± 1.4 kbar) to the staurolite-kyanite zone (567 ± 105°C and 6.7 ± 1.6 kbar). These data are combined with previous studies to modify a two-stage conceptual model for the thermal and deformation conditions of the middle and upper crust during the Eocene-Miocene, excluding the late Miocene to recent. In the Miocene (~23 Ma), Barrovian metamorphism was overprinted by decompression during coeval south directed extrusion of the Greater Himalayan Series beneath the Sangla detachment in the foreland and doming during top-down-to-the-west displacement along the Leo Pargil shear zone in the hinterland. These data demonstrate that shear zones and detachments, such as the South Tibetan detachment that initially formed during crustal thickening (e.g., Eocene-Oligocene), contributed to the subsequent distribution of rocks that experienced different pressure-temperature-time paths, degrees of partial melting, and exhumation histories during the Miocene.

1. Introduction

The Himalaya formed as a result of the collision between the Indian and Eurasian plates [*Gansser*, 1964], initiating in the Paleocene [e.g., *Zhuang et al.*, 2015] and continuing today [*Bilham et al.*, 1997; *Bettinelli et al.*, 2006]. In the NW Himalaya, subduction of the Indian plate thickened the crust via formation of the North Himalayan nappes at 50–40 Ma [e.g., *Guillot et al.*, 2003; *Epard and Steck*, 2008]. Barrovian metamorphism ensued in the middle crust during the late Eocene and early Oligocene [*Steck et al.*, 1993; *Vance and Harris*, 1999; *Steck*, 2003; *Chambers et al.*, 2009; *Langille et al.*, 2012, 2014], while a fold and thrust belt, composed of passive Indian margin rocks within the Tethyan Sedimentary Series (TSS), formed in the upper crust [*Searle*, 1986; *Searle et al.*, 1990; *Steck et al.*, 1993; *Wiesmayr and Grasemann*, 2002]. The formation of thickened crust, shear zones, and detachments during these early orogenic stages (e.g., Eocene and Oligocene), in many cases, exerted a strong control on the subsequent localization of midcrustal flow, partial melting, extrusion, and exhumation that characterized the Miocene [e.g., *Steck*, 2003].

Many models propose that the contact between the TSS and the high-grade core of the Himalaya (Greater Himalayan Series; GHS) initially formed during thrusting [*Burg et al.*, 1984a, 1984b; *Burchfiel et al.*, 1992; *Ratschbacher et al.*, 1994; *Dèzes et al.*, 1999; *Godin et al.*, 1999]. It is the principal surface (e.g., South Tibetan detachment system; STDS) for differential displacement between the TSS and GHS in several geodynamic models for the Himalaya [*Burg et al.*, 1984a; *Burchfiel and Royden*, 1985; *Burchfiel et al.*, 1992; *Grujic et al.*, 1996; *Beaumont et al.*, 2001; *Hodges et al.*, 1996, 2001; *Vannay and Grasemann*, 2001; *Yin*, 2006; *Webb et al.*, 2007, 2011]. The STDS also plays a critical role in models for the formation of domes that are cored by the GHS. The Gianbul dome in Zanskar was formed during reactivation of the TSS-GHS contact [*Robyr et al.*, 2002, 2006; *Horton et al.*, 2014]. For North Himalayan gneiss domes that are cored by GHS and mantled by TSS, this contact initially formed the upper surface of the southward extruding, high-grade core that was domed

synextrusion or postextrusion [*Nelson et al.*, 1996; *Hauck et al.*, 1998; *Lee et al.*, 2000, 2004, 2006; *Aoya et al.*, 2006; *Quigley et al.*, 2006, 2008; *King et al.*, 2007; *Lee and Whitehouse*, 2007; *Langille et al.*, 2010; *Larson et al.*, 2010].

In many parts of the Himalayan orogen, crustal thickening resulted in metamorphism that was followed by exhumation of midcrustal rocks [*Godin et al.*, 2001]. Movement along localized zones of rheological contrasts (e.g., TSS-GHS) [*Burg et al.*, 1984a; *Vannay and Grasemann*, 2001; *Wiesmayr and Grasemann*, 2002; *Searle and Godin*, 2003; *Searle*, 2010] enabled muscovite dehydration melting [*Inger and Harris*, 1992; *Harris et al.*, 1995; *Patiño Douce and Harris*, 1998] as a result of shear heating [*Harrison et al.*, 1999; *Nabelek et al.*, 2010] and decompression [*Harris and Massey*, 1994]. There is also the potential of water-fluxed melting in some portions of the GHS [*Weinberg and Hasalová*, 2015]. Partial melting decreases the bulk viscosity of the midcrust (e.g., GHS), making it weaker than the upper and lower crust. These conditions, in combination with lateral pressure gradients, such as those observed between the Tibetan plateau and the foreland, can result in channel flow as has been proposed for movement of the GHS between the STDS and Main Central thrust (MCT) [*Beaumont et al.*, 2001; *Grujic et al.*, 2002; *Godin et al.*, 2006].

The structural contact between the GHS and TSS occurs along orogenic strike, including Bhutan (e.g., Chekha Formation), Nepal (e.g., Annapurna Formation), and NW India (e.g., Haimanta Group and Phe Formation) [*Yin*, 2006]. Locations that preserve snapshots of the TSS-GHS contact during the Eocene-Oligocene are opportunities to characterize the thermal and rheologic conditions at this boundary during the early stages of the orogen [*Chambers et al.*, 2009; *Kellett and Grujic*, 2012; *Stübner et al.*, 2014]. Other areas of the Himalaya that were overprinted by melting and high-temperature, moderate-pressure metamorphism during the Miocene are critical for testing the relationship between strain localization, partial melting, midcrustal flow, and exhumation following the Eocene-Oligocene [*Hodges*, 2000; *Searle et al.*, 2003; *Jessup et al.*, 2008; *Kellett et al.*, 2010].

Within a 26 km long transect exposed in the Sutlej Valley, NW India, the Haimanta Group preserves a record of Oligocene deformation and metamorphism (Figure 1). During the Miocene, the margins of the transect were overprinted by the formation of the Leo Pargil dome (LPD) in the hinterland and extrusion of the GHS in the foreland [*Vannay and Grasemann*, 1998, 2001; *Vannay et al.*, 2004; *Chambers et al.*, 2008, 2009; *Langille et al.*, 2012]. We use this opportunity to contrast two snapshots of the thermal and deformation conditions during the evolution of the Himalaya: (1) upper crustal deformation and Barrovian metamorphism during the Eocene-Oligocene and (2) decompression in response to doming of the LPD and extrusion below the STDS during the Miocene. The tectonic evolution of the midcrust between the Miocene to recent was excluded from these models.

This transect was selected because of the following assets. First, pressure-temperature-time-deformation (*P-T-t-D*) paths are well constrained [*Vannay and Grasemann*, 1998, 2001; *Grasemann et al.*, 1999; *Vannay et al.*, 1999, 2004; *Thiede et al.*, 2006; *Leech*, 2008; *Chambers et al.*, 2009; *Langille et al.*, 2012, 2014; *Lederer et al.*, 2013]. Second, a parallel transect in Pin Valley, located west of Sutlej Valley, records structurally higher crustal positions where brittle deformation dominated in the upper crust at anchizone conditions by 45 Ma [*Wiesmayr and Grasemann*, 2002; *Neumayer et al.*, 2004]. These crustal depths can be combined with Barrovian metamorphism in the middle crust that is exposed within the deep gorges of the Sutlej River. Third, the Haimanta Group on both ends of the transect was overprinted by deformation fabrics and metamorphic phases that record decompression during formation of the LPD [*Thiede et al.*, 2006; *Langille et al.*, 2012, 2014] to the NE and extrusion below the local equivalent of the STDS to the SW [*Vannay and Grasemann*, 2001; *Vannay et al.*, 2004].

Our new field- and laboratory-based structural data and pressure-temperature (*P-T*) estimates test for field gradients in strain and metamorphism on the southern margin of LPD. A correlation between these data and the *P-T-t-D* evolution of rocks from the MCT to the LPD are the foundation for a conceptual model of the tectonic evolution of the region that was adapted from *Wiesmayr and Grasemann* [2002] and *Vannay et al.* [2004]. This is used to explore possible relationships between deformation, partial melting, and localized midcrustal flow.

2. Geologic Background

The Himalaya of NW India was created through a series of events, beginning with collision during the late Paleocene and early Eocene, and resulting in several orogenic phases [*Gansser*, 1964; *Hodges*, 2000; *Yin and Harrison*, 2000; *Steck*, 2003; *Yin*, 2006]. The Transhimalayan batholith phase [*Steck*, 2003] or Protohimalayan phase [*Hodges*, 2000] involved subduction of oceanic lithosphere beneath the Asian plate and the creation
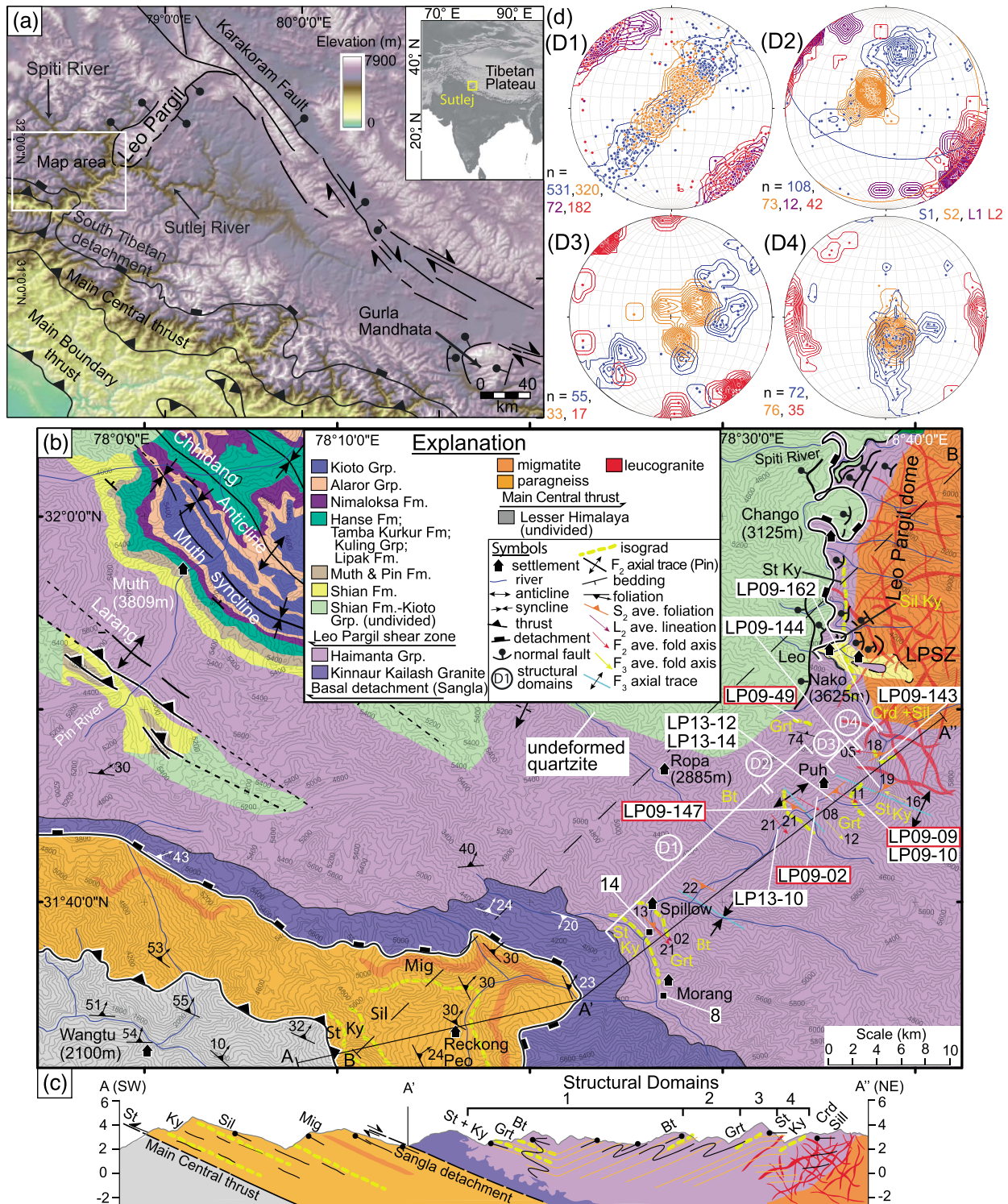
Figure 1. (a) Digital elevation map (USGS GTOPO30) of the Himalaya and Tibetan plateau modified after *Langille et al*. [2012]. (b) Simplified geologic map of the Spiti, Pin, and Sutlej Rivers, NW India modified after *Wiesmayr and Grasemann* [2002], *Vannay et al*. [2004], *Thiede et al*. [2006], *Caddick et al*. [2007], *Chambers et al*. [2009], and *Webb et al*. [2011]. Structural data from *Vannay et al*. [2004] are shown as white or black. Representative structural data, collected during this investigation, are shown for transect. White brackets define structural domains (D1–D4). (c) Geologic cross section of the Sutlej Valley section includes data from the Main Central thrust (MCT) to Sangla detachment (SD) [*Vannay et al*., 2004], hanging wall to the SD [*Caddick et al*., 2007; *Chambers et al*., 2009], and the Leo Pargil dome [*Thiede et al*., 2006; *Langille et al*., 2012, 2014]. (d) Stereonets for Domains 1–4: blue, S1; orange, S2; purple, L1; red, L2. Plots created using Stereonet v. 8.7 [*Allmendinger et al*., 2013]. Heavy dashed line defines the cross-section line of *Vannay et al*. [2004] that is used to for compilation of data in Figure 9. Dashed yellow line denotes approximate transitions between metamorphic zones.

of the Ladakh batholith during the late Cretaceous and Paleocene [*Weinberg and Dunlap*, 2000]. The Indus-Yarlung suture zone, composed of fragments of ophiolites and flysch, defines the contact between the Transhimalayan batholith to the north and the rocks of the Indian plate to the south [e.g., *Steck*, 2003].

Timing for collision can be inferred from a range of stratigraphic, paleomagnetic, and metamorphic data (summary in *Zhuang et al.* [2015]). Detrital zircon U-Pb data and fission track ages, combined with Nd and Sr isotopes, indicated that collision in the western Himalaya initiated during the Paleocene and ended by 50 Ma [*Zhuang et al.*, 2015]. The timing of collision can also be inferred from the end of marine sedimentation and the beginning of crustal shortening [e.g., *Searle et al.*, 1987, 1997]. The deceleration of convergence at ~50 Ma constrains the timing for the onset of the subduction of the Indian plate beneath Eurasia [e.g., *Molnar and Stock*, 2009]. Ages of subduction, as inferred from eclogite metamorphism in Tso Morari dome, NW India, range between 58 and 43 Ma [*de Sigoyer et al.*, 2000, 2004; *Leech et al.*, 2005, 2007; *St-Onge et al.*, 2013] (summary in *Donaldson et al.* [2013]). However, collision may have occurred earlier [*Yin and Harrison*, 2000] and episodically [*White and Lister*, 2012].

A series of thrust sheets and/or nappes were juxtaposed as thrusting migrated toward the foreland (Figure 1) [*Steck*, 2003]. The structurally higher positions of the Himalaya consist of the TSS rocks that were deposited on the Indian margin during the Precambrian-Eocene [*Steck*, 2003]. Deeper structural positions, including thrust sheets and/or nappes that were derived from the upper margin of the Indian plate, are part of the North Himalayan nappes [e.g., *Guillot et al.*, 2003; *Epard and Steck*, 2008]. These record crustal thickening and Barrovian metamorphism during the Eocene-Oligocene (e.g., North Himalayan phase or Eohimalayan phase) [*Hodges*, 2000; *Steck*, 2003].

The GHS, also known as the Higher Himalayan Crystalline Series, represents a deeper structural position of Proterozoic-Cambrian rocks that were metamorphosed, partially melted, and injected by leucogranites during the late Oligocene-Miocene (e.g., High Himalayan phase or Neohimalayan phase) [*Hodges*, 2000; *Steck*, 2003]. The STDS tectonically juxtaposed the upper margin of GHS with the TSS [*Searle*, 1986; *Dèzes et al.*, 1999; *Vannay and Grasemann*, 2001]. The MCT separates Proterozoic rocks of the Lesser Himalayan Crystalline Series (LHCS) in the footwall and GHS in the hanging wall [*Steck*, 2003]. The Main Boundary thrust tectonically separated the LHCS, along with metasedimentary rocks of the Lesser Himalaya, from the Neogene and Quaternary sedimentary units that were eroded from the Himalaya and deposited in the foreland basin (Subhimalaya) [*Steck*, 2003].

3. Regional Geology

In the Spiti-Lingti Valleys (Figure 1b), SW vergent nappe formation in the passive Indian margin sedimentary rocks record 30–36% of crustal shortening during the Eocene that resulted in an axial planar foliation at ~45 Ma [*Wiesmayr and Grasemann*, 2002; *Neumayer et al.*, 2004]. At deeper structural positions, a penetrative schistosity records an early stage of thin-skinned thrusting, followed by SW directed thrusting in the Haimanta Group [*Vannay et al.*, 2004] and overlying units [*Wiesmayr and Grasemann*, 2002].

The Haimanta Group (Precambrian-Cambrian) is a sequence of metagraywackes, metapelites, and metasilt-stones (Figure 1). It is alternatively interpreted as part of the GHS [*Steck*, 2003] or TSS [*Webb et al.*, 2011]. These units are capped by fan conglomerates and quartzite of the Ordovician age Shian Formation (950 m), the Silurian age Pin Formation (280 m), and the Devonian age Muth Formation (260 m). A younger sequence extends for >2 km (Figure 1b) [*Fuchs*, 1982]. The Haimanta Group extends for >6250 m deeper to the upper surface of the Sangla detachment (SD), as defined by restoration of balanced cross sections [*Wiesmayr and Grasemann*, 2002; *Neumayer et al.*, 2004].

The modern exposure of the SD, the local equivalent of the STDS, defines a transition zone between the Paleozoic (488 Ma) Kinnaur Kailas granite (aka Akpa granite) [*Miller et al.*, 2001] at the base of the Haimanta Group and migmatitic paragneiss of the GHS (Figures 1b and 1c). An early phase of mylonite development on the SD records foreland-directed thrusting [*Vannay et al.*, 2004]. Top-down-to-the-northeast shear sense that overprinted early south directed thrusting records reactivation during general shear within a compressional extensional stretching fault that accommodated southward extrusion of the GHS [*Vannay and Grasemann*, 2001; *Vannay et al.*, 2004]. When projected to the NE, the footwall of the SD at the base of the Tethyan + Haimanta fold and thrust belt transitions from GHS to North Himalayan crystalline series (NHCS) [*Wiesmayr and Grasemann*, 2002].

The GHS extends for a ~10 km structural thickness below the SD, where it is bounded by the NE dipping MCT that accommodated a minimum of 100 km of displacement during SW directed thrusting (Figures 1b and 1c) [*Vannay and Grasemann*, 1998, 2001; *Vannay et al.*, 2004; *Chambers et al.*, 2008; *Webb et al.*, 2011; *Leger et al.*, 2013; *Law et al.*, 2013]. Following extrusion between the SD and MCT (23–16 Ma), thrusting in the footwall of the MCT resulted in decreased exhumation rates of the GHS (15–2 Ma) [*Vannay and Grasemann*, 2001; *Thiede et al.*, 2009]. A relatively isobaric (8 kbar) inverted metamorphic field gradient (570–750°C) begins at the staurolite isograd above the MCT (Figure 1c), continuing to the second sillimanite isograd and associated partial melt zone near the SD [*Vannay and Grasemann*, 1998, 2001]. Temperatures of 750°C at the top of the GHS resulted in partial melting [*Vannay et al.*, 2004].

North of the SD, the Haimanta Group contains kyanite and staurolite at the deepest structural position (Figure 1b) of a metamorphic field gradient that decreases to the biotite zone toward structurally higher positions [*Vannay et al.*, 2004; *Chambers et al.*, 2009]. Within the lower portion of the Haimanta Group, as exposed near Morang (Figure 1b), prograde Barrovian metamorphism (615 ± 5°C; 7–8 kbar) resulted in garnet growth (>34–28 Ma) and maximum burial at ~30 Ma [*Chambers et al.*, 2009]. Kyanite and staurolite growth (640–660°C; 6–7 kbar) occurred during a slight decompression stage [*Chambers et al.*, 2009].

The LPD is an elongate, NE striking domal structure (Figures 1a–1c) located ~34 km NE of the SD. The Leo Pargil and Qusum shear zones bound the LPD on the NW and SE sides, respectively [*Zhang et al.*, 2000; *Thiede et al.*, 2006; *Langille et al.*, 2012]. The dome contains a carapace of the Haimanta Group that was intruded by an extensive network of dikes and sills between 30 and 18 Ma [*Thiede et al.*, 2006; *Leech*, 2008; *Lederer et al.*, 2013]. Staurolite and kyanite in rocks from the village of Puh and the LPD indicate that they reached ~530–630°C and ~7–8 kbar during Barrovian metamorphism (Figures 1b and 1c) that ceased at 29–27 Ma [*Langille et al.*, 2012]. The central portion of the dome is composed of migmatitic gneiss, which was dominated by melt-present deformation and formed during a semicontinuous period of partial melting between 30 and 18 Ma [*Langille et al.*, 2012; *Lederer et al.*, 2013]. These rocks were alternatively interpreted as part of the GHS [*Neumayer et al.*, 2004] or the NHCS [*Vannay and Grasemann*, 2001; *Vannay et al.*, 2004; *Wiesmayr and Grasemann*, 2002].

Hintersberger et al. [2011] proposed the following six stages of deformation to characterize the evolution of faults for a portion of NW India in which the LPD is located: D1, NE-SW (arc-normal shortening); D2, ENE-WSW shortening; D3, NE-SW (arc-normal) extension; D4, NW-SE (arc-parallel extension); D5, N-S shortening; and D6, E-W extension. For the SW margin of the LPD, *Thiede et al.* [2006] proposed that D1 created a foliation and lineation. Shear bands (D2), brittle-ductile faults (D3), and brittle faults (D4) overprinted these fabrics. Ductile extensional shear bands (e.g., D2 of *Thiede et al.* [2006]), which record top-down-to-the-west, postdated Barrovian metamorphic porphyroblasts [*Langille et al.*, 2012]. D4 brittle faults of *Thiede et al.* [2006] are the equivalent to D6 faults of *Hintersberger et al.* [2011].

The Leo Pargil shear zone (LPSZ), in the southwestern portion of the dome (Figure 1b), is composed of interlayered schist, quartzite, and marble that contains a penetrative west dipping foliation with a downdip stretching lineation [*Thiede et al.*, 2006; *Langille et al.*, 2012, 2014]. Since marble and quartzite do not occur in the Haimanta Group [*Fuchs*, 1982], these probably represent a stratigraphic position above the Haimanta Group equivalent to the Shian, Muth, and/or Pin Formation [*Thiede et al.*, 2006]. Mesoscale and microscale shear sense indicators record top-down-to-the-west sense of shear [*Thiede et al.*, 2006; *Langille et al.*, 2014]. Quartz microstructures constrain shearing at deformation temperatures ranging from >650°C to 280°C, with highest deformation temperatures in the migmatite core and lower temperatures overprinting higher temperatures during exhumation (see *Langille et al.* [2014] for details). The ductile shear zone juxtaposed metamorphic rocks of the leucogranite injection complex in the dome with variably metamorphosed rocks in the hanging wall [*Langille et al.*, 2012, 2014]. Between 10 and 6 Ma, initiation of movement on the north striking Kaurik-Chango normal fault, a steep brittle fault located on the SW corner of the LPD that also contributed to its exhumation, resulted in top-down-to-the-west displacement of the ductile LPSZ during D6 of *Hintersberger et al.* [2011].

By comparing exhumation rates for the Haimanta Group (1.3 mm/yr), located in the hanging wall of the SD, with exhumation rates from the GHS (2.2 to 3.0 mm/yr), *Chambers et al.* [2009] proposed that the Haimanta Group was decoupled from the southward extruding GHS by 23 Ma. This supports models for extrusion of the GHS between the MCT and SD from 23 to 16 Ma [*Vannay and Grasemann*, 2001]. NE of the SD

(~34 km), beyond a zone of the Haimanta Group where Oligocene deformation and metamorphism are preserved, sillimanite and cordierite overprinted prograde assemblages in the Haimanta Group during doming and near-isothermal decompression [*Langille et al.*, 2012]. Between the end of Barrovian metamorphism (29 Ma) and the onset of decompression (>23 Ma), accommodated by the LPSZ, exhumation rates of the LPD were ~1.3 mm/yr [*Langille et al.*, 2012].

4. Objectives

Only a few systematic assessments of the transition zone from the Haimanta Group in the Sutlej Valley to the LPD existed prior to this investigation, including isograds and *P-T-t-D* paths [*Vannay et al.*, 2004; *Caddick et al.*, 2007; *Chambers et al.*, 2009; *Langille et al.*, 2012], foliations and lineations in the SW portion [*Vannay et al.*, 2004], and mesoscale structures [*Webb et al.*, 2011]. The main objectives of this investigation are to (1) document mesoscale structures from the SD to the LPD, (2) characterize microstructures from the biotite zone to the cordierite-sillimanite zone near the LPD, (3) constrain the relative timing between porphyroblast growth of metamorphic index minerals and deformation, (4) test for gradients in strain and metamorphism from the biotite zone to the injection complex that bounds the LPD, and (5) add data that were published post-2004 to extend the compilation of *P-T-t* data from *Vannay et al.* [2004] NE through the dome. These new constraints are used to modify conceptual tectonic models, proposed by *Vannay et al.* [2004] and *Wiesmayr and Grasemann* [2002], by adding details from previous investigations [*Neumayer et al.*, 2004; *Leech*, 2008; *Chambers et al.*, 2009; *Langille et al.*, 2012, 2014; *Lederer et al.*, 2013]. The models are used to reevaluate crustal thickening, Barrovian metamorphism, partial melting, and the role of older Eocene structures in the Miocene exhumation history. By fulfilling these objectives, this contribution characterized the conditions of the SD and LPSZ during upper crustal and midcrustal processes that contributed to the geodynamic evolution of the orogen.

5. Mesoscale Structures in the Haimanta Group

5.1. Sequence of Deformation Events as Proposed by *Vannay et al.* [2004]

Detailed structural measurements from the lower positions of the Haimanta Group in the hanging wall of the SD, exposed along the Sutlej Valley [*Vannay et al.*, 2004], are used to calibrate the new structural data presented in this manuscript. An early phase of isoclinal folding (F1) was responsible for the main schitosity (S1) that is oriented subparallel to compositional layering (S0) in the lower section of the Haimanta Group [*Vannay et al.*, 2004]. A second NW striking penetrative schitosity (S2), defined as the axial planar surface to SW verging folds, contains a NE trending, shallowly plunging mineral lineation (L2) [*Vannay et al.*, 2004]. Two deformation events were interpreted to record an early stage of thin-skinned thrusting followed by SW directed thrusting and folding in the Haimanta Group [*Vannay et al.*, 2004] and the shallower units above [*Wiesmayr and Grasemann*, 2002]. The similar orientation between S2 and mylonite zones in the GHS was attributed to SW directed extrusion that was accommodated by the SD and MCT [*Wiesmayr and Grasemann*, 2002].

5.2. New Mesoscale Data for the Sutlej Valley

Orientation data from foliation surfaces, crenulation cleavages, fold hinges, and intersection lineations were collected along the 28 km long transect between the staurolite-kyanite zone in the hanging wall of the SD and the LPD. Different generations of structures were documented at each stop. The relative overprinting of fabrics for each outcrop established a sequence of deformation. Structures within the Haimanta Group were divided into four domains that contain relatively consistent sets of structural data (Figures 1b–1d). A pervasive foliation (S1) was folded by at least two generations of folds (F2 and F3). Subhorizontal, NW trending F2 fold hinges with an axial planar foliation (S2) are present in many outcrops [*Chambers et al.*, 2009]. The intersection between S1 and S2 created a prominent intersection lineation (L2) with an orientation that is parallel to F2 fold hinges. The structures related to D2 were refolded by at least one additional generation of open, upright folds (F3), which generally trend NW.

5.2.1. Domain 1

Domain 1 extends from Morang to ~4 km SW of the village of Puh (Figures 1 and 2). The SW portion of the transect overlaps with the area of previously documented structural data [*Vannay et al.*, 2004; *Webb et al.*, 2011] and detailed *P-T-t-D* paths [*Chambers et al.*, 2009] at the base of the Haimanta Group. This domain is characterized by S1 foliation that was folded by subhorizontal, NW trending F2 folds (Figures 1d and 2). An axial planar S2 was preserved as a crenulation cleavage. The intersection between S2 and S1 creates a NW
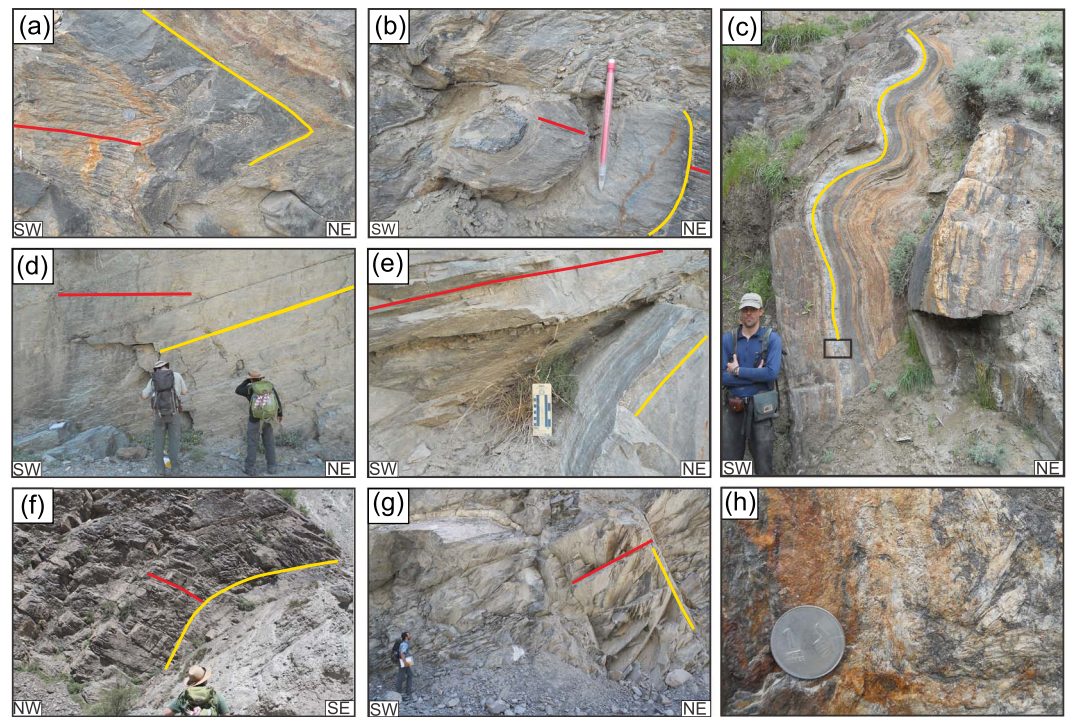
Figure 2. Representative mesoscale structures on the NE (Figures 2a–2c) and SW (Figures 2d–2g) dipping limbs of the F3 synform in Domain 1. (a) S1 (yellow) was folded by F2 (18° → 320°) with an S2 (290°, 24° NE) crenulation cleavage (red): 31.6085°N, 78.4357°E. One Indian Rupee coin (25 mm diameter) is for scale. (b) S1 (yellow) folded by F2 (15° → 316°) with an S2 axial planar cleavage (306°, 35° NE). S1 contains layers with staurolite that were folded by F2: 31.6333°N, 78.4298°E. (c) S1 (315°, 85° SW near hinge) was folded by F2: 31.6085°N, 78.4357°E. (d) The southwesternmost portion of SW dipping limb of F3 synform with exposures of S1 (yellow; 312°, 35° SW) and S2 (red; 288°, 11° SW). (e) F2 fold with crenulation on the hinge area (11° → 133°). S1 (yellow; 312°, 35° SW) was folded by F2 with an S2 surface (red; 288°, 11° SW). Location for Figures 2d and 2e: 31.6698°N, 078.4730°E. (f) View across Sutlej River of SW dipping S2 (red) with S1 (yellow) folded by F2 near the northeasternmost portion of Domain 1. (g) Same location as Figure 2f but viewed in the opposite direction where S1 (yellow; 305°, 65° NE) is oriented at a high angle to S2 (red; 325°, 26° SW). Location of Figures 2f and 2g: 31.7241°N, 078.5481°E. (h) Enlargement of 15 cm thick layer that is composed of interlocking blades of kyanite shown as black rectangle in Figure 2c. One Indian Rupee coin (25 mm diameter) is for scale. Viewing surface for all outcrops is vertical.

trending L2 intersection lineation that is subparallel to the F2 fold hinges (Figure 1d). Poles to the majority of S2 cluster in two maxima that are the product of the NE (Figures 2a–2c) and SW dipping limbs (Figures 2d–2g and 3a) of F3 folds (Figure 1d). Blades of kyanite grew randomly on S1 (Figure 2h). The area of inflection near this southernmost synform, where the S2 foliation becomes horizontal ~ 1 km NE of Spillow, roughly coincides with the biotite zone [*Chambers et al.*, 2009]. Together these define a right way-up sequence of isograds from kyanite to biotite between Morang and Spillow [*Chambers et al.*, 2009]. *Chambers et al.* [2009] proposed that the majority of kyanite and staurolite growth occurred after crenulation cleavage (their D2) and during a slight modification of S2.

5.2.2. Domain 2

The SW extent of Domain 2 is defined by an open, upright F3 antiform, which deflects the consistent orientations of Domain 1 (Figure 1d). Near Puh, garnet porphyroblasts are concentrated along S2, and these define the garnet zone on the NE limb of the F3 synform (Figure 3b). S1 forms a strong maximum, including data from the SW limb (Figure 1d). S2 in this region defines a strong maximum that is defined by a SE dipping limb (Figure 1d). Intersection of S1/S2 (L2) is subparallel to F2 fold hinges (Figure 1d). Kyanite blades are randomly oriented on S1 (Figure 3c). Staurolite porphyroblasts are randomly oriented on S2 (Figure 3d) and S1 surfaces (Figure 3e), suggesting that their growth postdated the majority of S2. The SW limb of an F3 antiform is located near the bridge on the SW portion of Domain 3 where S2 is shallow and SE dipping (Figure 3f).

5.2.3. Domain 3

Domain 3 contains garnet, staurolite, and kyanite porphyroblasts within a prominent F3 antiform (Figure 1d). The F3 antiform, located between two bridges near the village of Dubling, is defined by the orientations of
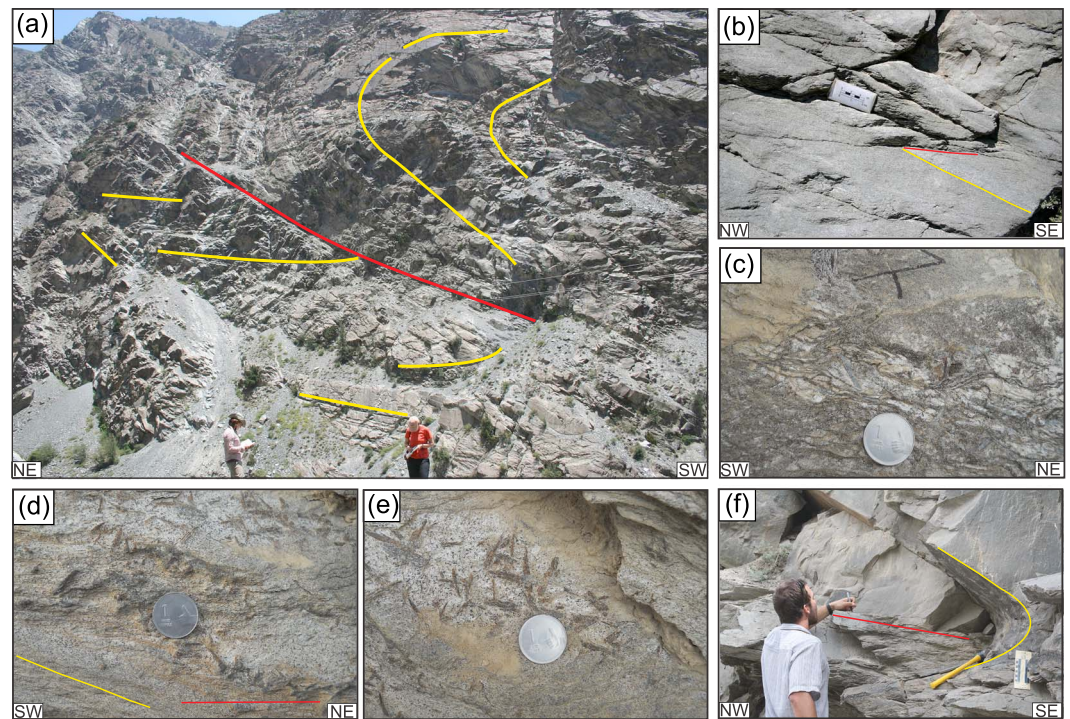
Figure 3. Representative mesoscale structures from between the northeasternmost position of Domain 1 and Domain 2. (a) S1 (yellow) is folded by F2 folds with SW dipping S2 (red). View toward the north of a ~300 m high vertical wall located across the Sutlej River. Representative of structures on SW dipping limb of F3 synform in the biotite zone: 31.7145°N, 78.5423°E. (b) Garnet-bearing schist with SE dipping S1/S2. Location of samples LP09-09 and LP09-10: 31.75217°N, 78.61956°E. (c) View of kyanite and staurolite porphyroblasts in sample LP13-14. Kyanite is randomly oriented on S1 surface (104°, 65° SW): 31.7570°N, 078.5977°E. (d) Oblique view of randomly oriented staurolite porphyroblasts on intersecting S1 (yellow; 105°, 56° SW) and S2 (red). Intersection of S1 and S2 creates L2 (00° → 105°). (e) View of staurolite on S1 surface (perpendicular to Figure 3d). Staurolite is randomly oriented on S1 and S2 surfaces: 31.7567°N, 78.5985°E. (f) Garnet-bearing S1 (yellow) is folded by F2 (08° → 333°) with S2 (red) axial surface 46°, 09° SE: 31.752°N, 78.6185°E.

S1, S2, and L2. Cliffs that extend above the road where the fold crosses the southern bridge expose the SW limb (Figure 4a). Near this bridge, the S1/S2 foliation dips SW (Figures 1d and 4b). The S2 maximum defines an average S2 orientation in the NE quadrant, while the orientation of S1 is more distributed. The corresponding limb of the F3 fold dips NW, creating a maximum of S2 poles in the SE quadrant and associated S1 orientations (Figures 1d and 4c). The majority of L2 intersection lineations are shallow plunging and NW trending. Kyanite and staurolite porphyroblasts are randomly oriented when viewed parallel or perpendicular to S1 (Figures 4e and 4f).

5.2.4. Domain 4

In contrast to Domains 1–3 where F2 folds trend NW, the majority of F2 fold hinges in Domain 4 (Figure 1d) trend E-W, while S1 and S2 dip north (Figure 5). Aside from a few measurements, the majority of poles to S1/S2 are in the southern domain. The S1 foliations are generally E-W striking and north to NW dipping. Shallow E-W plunging fold hinges close around an E-W striking S2 axial surface (Figure 1d). In these F2 hinges, exposures of steeply dipping S1 intersect north (Figure 5a) and south (Figure 5b) dipping S2 (Figure 1b). Poles to S2 define a maximum in the SE. The south dipping S2 observed in outcrops (Figure 5b) is also supported by the south dipping S2 measurements (Figure 1d). The majority of L2 are shallowly plunging and E-W trending. The distribution of staurolite and kyanite porphyroblasts, when viewed on S1, is random (Figure 5c).

Domain 4 marks the first exposures of leucogranite dikes and sills located south of the LPD (Figure 5d). Here folds deform leucogranite dikes that were emplaced at a high angle to the west striking and north dipping foliation (Figure 5d). The fabric relationships, exposed dramatically within the walls of the Sutlej River gorge (Figure 5d), are also exposed at lower positions (Figure 5e). S1 and S2 dip north and are crosscut at a high angle by a leucogranite dike, which lacks internal solid-state fabrics (Figure 5e). Based on these relationships,
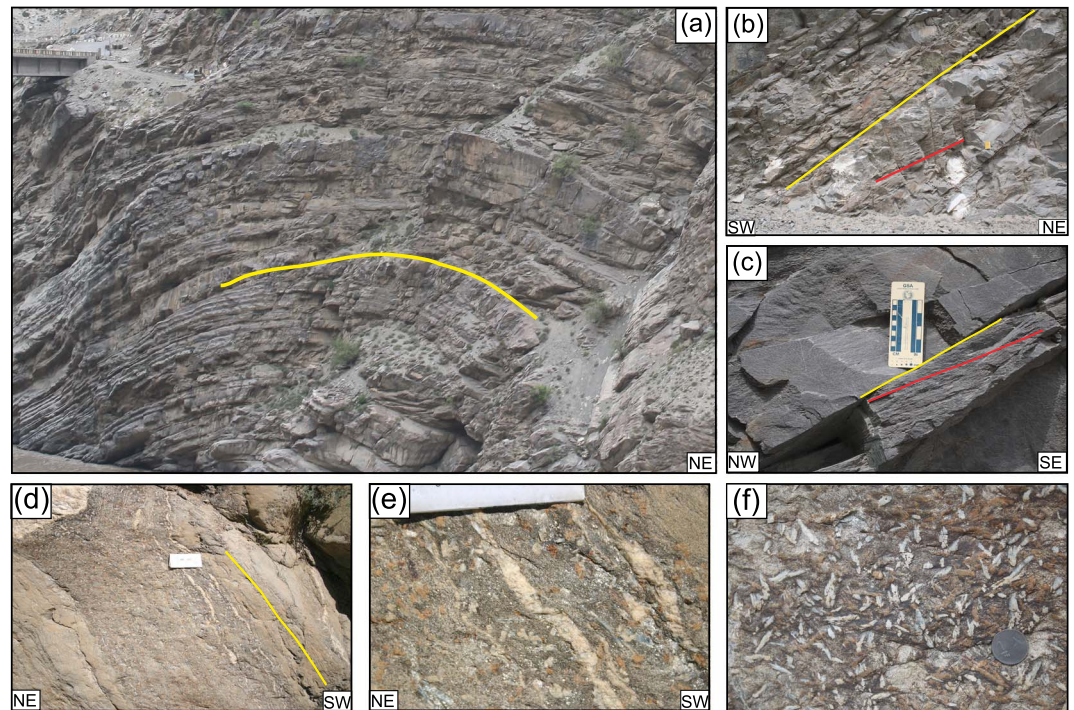
Figure 4. Representative mesoscale structures from Domain 3. (a) View toward the NW of bridge (upper left corner) near the town of Dubling within a region on the SW limb of an F3 antiform: 31.7523°N, 078.6305°E. (b) Vertical wall of staurolite schist on the SW limb of the Dubling antiform shows the intersection of S1 and S2 (red; 351, 14 SW), which are folded by F3: 31.7529°N, 78.6252°E. (c) Vertical exposure on bridge that is north of Dubling preserves S1 (yellow; 244°, 32° NW) and S2 (red; 070°, 20° NW) that record the north limb of the Dubling antiform: 31.767°N, 78.6376°E. (d) Kyanite and staurolite porphyroblasts viewed parallel to S1. Some elongate kyanite blades are partially aligned within S1 (yellow), while others are random. Exposure of the lower limb (S1; 151°, 50° SW) of an F2 fold with staurolite and kyanite porphyroblasts. Location of sample LP09-144: 31.7607°N, 078.6360°E. (e) Enlarged view of area shown on Figure 4d. (f) Kyanite blades are randomly oriented when viewed perpendicular to S1 surfaces.

the main fabric exposed on the gorge walls is interpreted to be composite S1/S2. Assuming that the folds record shortening perpendicular to S2, these could be interpreted as F2. Abundance of leucogranite increases toward the Spiti/Sutlej confluence, where leucogranite dikes/sills were deformed by folds that could potentially be F2 (Figures 5f and 5g). Leucogranite sills, emplaced parallel to S2, were displaced by a normal fault, while the surrounding schist was deflected (Figure 5h).

6. Microscale Structures and Metamorphic Zones

6.1. Garnet Zone

Representative samples from the garnet zone were collected from near the village of Puh within the Haimanta Group (Figure 1b). Samples LP09-147 (Figure 6a) and LP09-02 (Figure 6b) are from within the garnet zone in Domain 2 and contain the assemblage garnet + biotite + quartz + plagioclase. Aligned white mica and biotite define S1 and S2. Fine-grained chlorite and biotite are oriented roughly parallel to the S2 axial surface foliation of the fold (Figure 6a). Sample LP09-02 contains a foliated matrix (S2) composed of interlayered biotite and white mica alternating with quartz- and albite-rich domains (Figure 6b). The foliated matrix (S2) is deflected around garnet porphyroblasts, indicating that deformation continued after porphyroblast growth (Figure 6b). Subhedral garnet porphyroblasts contain ilmenite, apatite, quartz, biotite, and albite inclusions that preserve a planar Si fabric (Figure 6b). Because these straight inclusion trails cannot be traced into a matrix foliation with an established relative chronology, they are defined as (S_i). Ilmenite, apatite, rare monazite, and zircon occur throughout the matrix. Chlorite formed during retrograde replacement of biotite. Rare large chlorite porphyroblasts form at a high angle to the main foliation, indicating that it grew after the main D2 fabric-forming event. LP13-10 is a representative sample from within the biotite zone (Figure 6c).
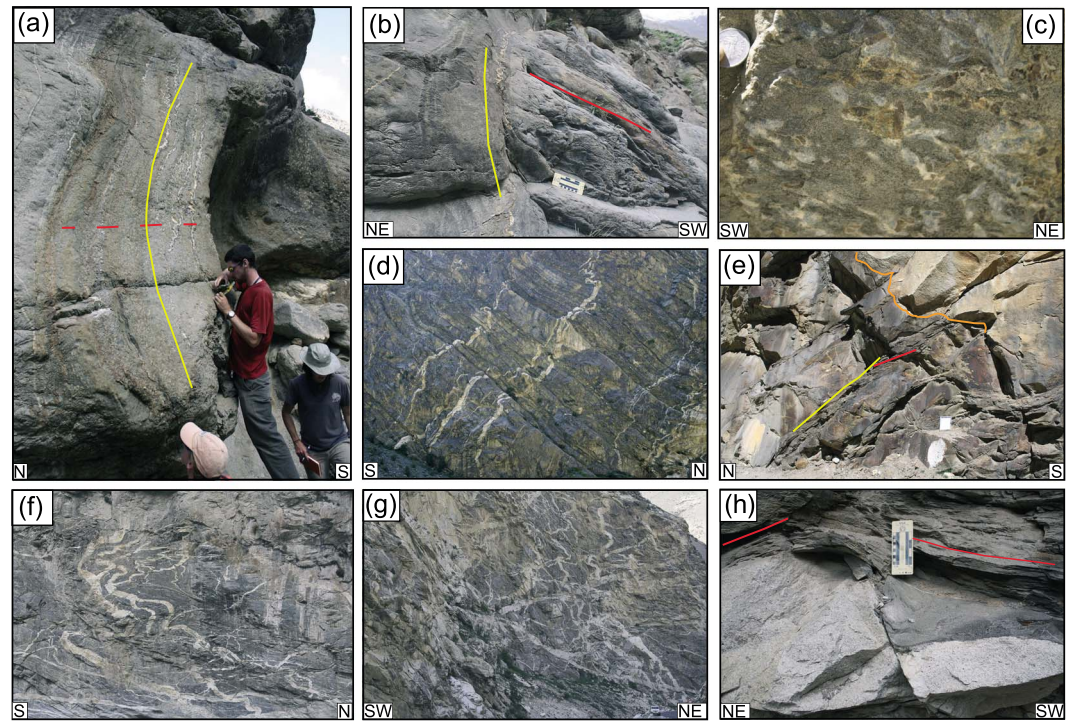
Figure 5. Representative mesoscale structures from Domain 4. (a) F2 (hinge; 12° → 095°; approximate axial surface; 095°, 31° NE) folds S1 foliation (yellow), containing kyanite and staurolite porphyroblasts. Outcrop is location of sample LP09-143. (b) View of S1 (yellow) with F2 ptygmatic folds (11° → 141°). S2 (red; 351°, 17° SW) forms at high angle to S1. (c) Slightly oblique view of S1 surface where the orientation of interlocking kyanite and staurolite porphyroblasts is random. One Indian Rupee coin (25 mm diameter) is for scale. Location of sample LP09-143: 31.7837°N, 078.6370°E. (d) Dikes viewed in ~300 m tall vertical wall that crosscuts main foliation (S1/S2 composite) in the southernmost portion of the injection complex: 31.7747°N, 078.6379°E. (e) Dip of S1 (yellow; 270°, 39° N) is slightly steeper than S2 (red; 085°, 31° NW). Leucogranite dike (orange) crosscuts the S1/S2 foliation at a high angle. A 40 × 45 cm map board for scale: 31.7921°N, 78.6355°E. (f) Approximately 100 m tall portion of a vertical wall with leucogranite dikes and sills that are folded: 31.8020°N, 078.6404°E. (g) Another view of injection complex near the confluence of the Spiti and Sutlej Rivers. White jeep in lower right corner provides scale. (h) Granite sill emplaced parallel to S2 (red; 082°, 15° NE), which is deflected around a portion of granite that was broken by fault plane (161°, 64° SW). At the mesoscale, the granite lacks any evidence for internal deformation: 31.8028°N, 078.6423°E.

6.2. Staurolite-Kyanite Zone

Staurolite and kyanite porphyroblasts coexist in outcrops just north of the village of Puh (Figure 7). Sample LP13-12A preserves the assemblage staurolite + chlorite + biotite + quartz + plagioclase + tourmaline + apatite. S1 foliation is defined by chlorite + biotite intergrowths and is folded by F2 folds and crenulations. Staurolite porphyroblasts contain sigmoidal inclusion trails that are continuous from the matrix to the grain (Figure 7a). These indicate that staurolite porphyroblasts overgrew F2 crenulations. The crenulation is slightly tighter in the matrix, suggesting growth late/syn crenulation. Sample LP09-09 contains the assemblage garnet + biotite + muscovite + plagioclase + quartz with staurolite present at the same outcrop. A pervasive S2 foliation is defined by aligned muscovite and biotite (Figure 7b). An earlier foliation (S1) is defined by alternating quartz- and mica-rich domains. Linear trails of quartz inclusions define a foliation (S_i) that predates the S1 foliation, but it cannot be directly linked to S1 (Figure 7b). Some staurolite-bearing samples (LP09-10) [see *Langille et al.*, 2012] contain elongate porphyroblasts that are inclined at an angle to the main foliation and contain strain shadows and strain caps composed of polygonal quartz (Figure 7c). The early foliation (S1) is transposed into the main foliation (S2). Polygonal quartz grain boundaries indicate static recrystallization through grain boundary area reduction [*Passchier and Trouw*, 2005].

LP13-14B contains the assemblage kyanite + biotite + chlorite + quartz + plagioclase. When viewed on surfaces cut perpendicular to the fold hinge, kyanite porphyroblasts contain sigmoidal S1 inclusion trails that are continuous with S1 in the matrix (Figure 7d). The crenulation is slightly tighter in the matrix. These
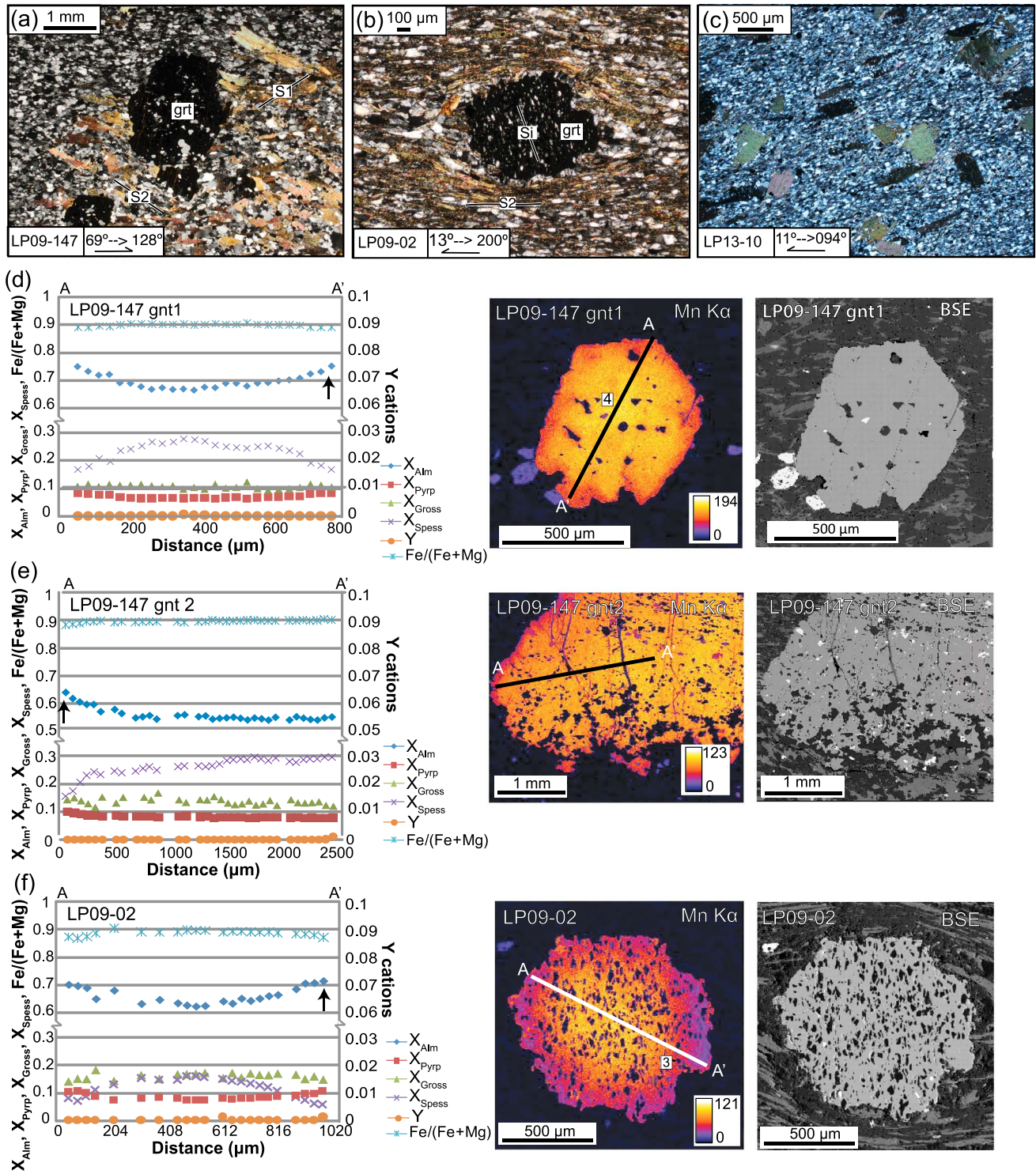
Figure 6. Representative microstructures and compositional data for garnet porphyroblasts collected from the garnet and the biotite zones. (a) Photomicrograph showing compositional layers defined by quartz- and feldspar-rich domains that are interlayed with phyllosilicate-rich layers near the hinge of an F2 fold. (b) Pervasive foliation (S2; 005°, 35° SE) is wrapped around a garnet porphyroblast. Linear inclusion trails define an early fabric (S_i). (c) Representative biotite schist from the biotite zone. (d and e) Compositional maps and analytical transects of representative garnet porphyroblasts in sample LP09-147. (f) Compositional map and analytical transect of representative garnet porphyroblast in sample LP09-02.
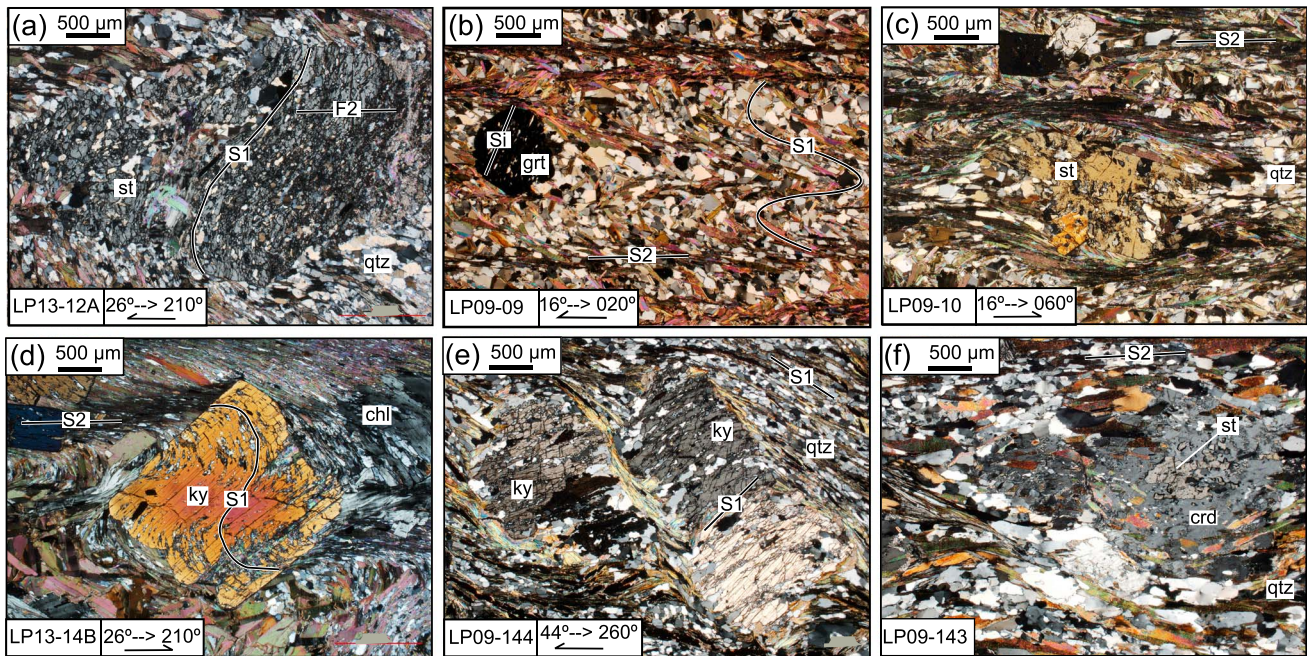
Figure 7. (a) Staurolite (st) porphyroblast with sigmoidal inclusion trails that define S1 continues into the matrix S1, indicating that staurolite overgrew F2. Cut perpendicular to L2: qtz, quartz: 31.758500°N, 78.597800°E. (b) Garnet (grt) porphyroblast that was collected from within the staurolite zone. S1 is folded by F2. See Figure 3b for field image. (c) Staurolite (st) porphyroblast that was rotated parallel to S2. Location of Figures 7b and 7c: 31.75217°N, 78.61956°E. (d) Kyanite (ky) porphyroblast with sigmoidal inclusion trails that indicate kyanite overgrew F2: Chl; chlorite: 31.757000°N, 78.597700°E. See Figure 3c for field image. (e) Kyanite (ky) porphyroblasts with inclusion trails that are continuous with the S1 foliation records another example of post F2 kyanite growth. Collected from the hinge of an F2 fold. See Figure 4d: 31.7607°N, 078.6360°E. (f) Cordierite (crd) overgrowths on staurolite (st) near the beginning of the injection complex. Sampled from the hinge zone of an F2 fold in Domain 4 (see Figure 5a): 31.783700°N, 78.637000°E.

indicate that kyanite formed late/syn F2 crenulations. In another example (LP09-144), which was cut parallel to the dip of the foliation, kyanite porphyroblasts overgrew linear inclusion trails that can be traced into the S1 fabric in the matrix (Figure 7e). These relationships provide additional evidence that kyanite overgrew F2 crenulations during D2 deformation. Quartz-rich layers contain polygonal grain boundaries between strain-free grains, indicating static recrystallization.

6.3. Cordierite-Sillimanite Zone

LP09-143 was collected near the first occurrence of leucogranite dikes and sills (Figure 5d) in an extensive injection complex. This sample contains the assemblage staurolite + plagioclase + cordierite + biotite + chlorite + quartz. The assemblage is a mix of prograde phases (staurolite) that were overprinted by a second stage of metamorphism (cordierite) through a reaction such as follows: $St + Ms + Chl + Qtz = Crd + Bt + H_2O$ [*Pattison et al.*, 1999]. The main foliation is defined by aligned biotite (Figure 7f). Chlorite forms splays that overgrow the foliation as well as aligned networks that are localized in shear bands. Subhedral to anhedral staurolite porphyroblasts are surrounded by overgrowths of cordierite. In areas with large sections of cordierite, the staurolite is small and anhedral. Synkinematic cordierite and sillimanite overgrowths on staurolite and kyanite are evidence for near-isothermal decompression at >23 Ma in the southern margin of LPD, which is located ~ 2 km north of this sample [*Langille et al.*, 2012]. Using the sequence of deformation proposed by *Hintersberger et al.* [2011], these shear zone fabrics are part D4 arc-parallel extension (NW-SE) [*Langille et al.*, 2014].

7. Mineral Chemistry

Mineral compositions for use in thermobarometric estimates were obtained using the Cameca SX-100 electron microprobe at the University of Tennessee, Knoxville. A PGT Si (Li) detector energy-dispersive spectrometer and electron backscatter imaging provided qualitative identification of phases during real-time analysis. X-ray compositional maps using a wavelength-dispersive spectrometer of Mg, Mn, and Ca, along with quantitative line

Table 1. Pressure-Temperature Estimates[a]

| | Peak | | | | | | Inclusions | | |
| | THERMOCALC | | | | | | | | |
Sample	T (°C)	P (kbar)	Assemblage	Removed	Cor.	Fit	Garnet-Biotite T (°C)	Garnet-Biotite T (°C)	Garnet-Ilmenite T (°C)
LP09-09	567 ± 105	6.7 ± 1.6	gnt + bt + mv + plg	—	0.80	0.09	593	—	549 ± 26(1)
									484 ± 27(2)
LP09-49	499 ± 99	4.5 ± 1.4	gnt + bt + mv + plg	fcel	0.78	0.37	578	—	—
LP09-02	571 ± 92	7.8 ± 1.4	gnt + bt + mv + plg	—	0.85	0.70	566	541 (3)	—
LP09-147gnt1	—	—	—	—	—	—	538	—	577 ± 21(4)
LP09-147gnt2	—	—	—	—	—	—	553	—	—

[a]THERMOCALC results calculated using the average PT mode. Numbers in parentheses correlate to the inclusion location boxes in Figures 6 and 8. Gnt-bt thermometer utilized the peak pressure estimated by THERMOCALC, with the exception that LP09-147 assumed 7 kbar.

transects across garnet porphyroblasts, were conducted at 15 kV, 30 nA, 30 ms, and a 6 μm spot size. Point chemical analyses at 15 kV, 20 nA, and a spot size of 1 μm were conducted on phases for calculating pressure-temperature (P-T) estimates and to test for compositional heterogeneities. Plagioclase grains were analyzed at 10 kV. Natural and synthetic compounds, used as standards, were checked before and after the analyses. Elemental abundances <300 ppm were considered undetectable. All raw microprobe data were reduced using the standard PAP software. Near-rim garnet compositions [*Kohn and Spear*, 2000] were combined with the biotite, muscovite, and plagioclase compositional data obtained from the microprobe. Biotite, muscovite, and plagioclase compositions in grains, located at various distances from the edge of the garnet, had little compositional variation, so these data were averaged for the P-T estimates.

The thermobarometric software THERMOCALC 3.33, with the updated *Holland and Powell* [1998] data set (tc-ds55. txt), was used to calculate P-T estimates from the chemical data [*Powell and Holland*, 1994] in average P-T mode. Activity coefficients for each phase were calculated using the software AX. The garnet-biotite Fe-Mg exchange thermometer using the *Holdaway* [2000] calibration and the garnet-ilmenite [*Pownceby et al.*, 1987, 1991] geothermometers were applied to garnet porphyroblasts that contained biotite or ilmenite inclusions to quantify metamorphic temperatures associated with an earlier portion of the garnet growth history. Errors for gnt-ilm data represent the range in temperatures calculated from the different calibrations. The garnet-biotite thermometer was used in conjunction with the peak pressure estimated by THERMOCALC, with the exception that LP09-147 assumed 7 kbar. Following *Holdaway* [2000], absolute error for sample LP09-147 is estimated as ± 25°C.

8. Garnet Zoning and Pressure-Temperature Estimates

8.1. Garnet Zone

LP09-147, within the SW portion of the garnet zone in Domain 2, contains resorbed relics of garnet that are concentrated along the inner region of biotite- and chlorite-rich domains, while subhedral garnet porphyroblasts are concentrated along the contact between the inner and outer domains (Figures 6a, 6d, and 6e). The foliation is defined by biotite, white mica, and albite. Garnet porphyroblasts that grew across compositional contacts contain opaque inclusions (Figure 6e). Inclusion-free, subhedral garnet porphyroblasts are distributed throughout the matrix (Figure 6d). Mn concentration decreases from core to near rim in garnet porphyroblasts despite the size (Figures 6d and 6e) and density of inclusions. The gradual decrease in Mn concentration in smaller garnets toward the rim and more abrupt decrease in the outer 250 μm of the larger grains are interpreted to record growth zoning profiles at this structural position. Smaller subhedral garnets (gnt1) and larger poikiloblastic garnets (gnt2) preserve growth zoning and yield temperature estimates of 538 ± 25°C and 553 ± 25°C, respectively (Figures 6d and 6e and Tables 1 and 2). Inclusions of ilmenite and garnet in the core of the garnet (Figure 6d, box 4, and Table 3) yield a temperature estimate of 577 ± 21°C and record an earlier higher temperature stage during prograde garnet growth.

In LP09-02, within the middle portion of the garnet zone, garnet porphyroblasts are subhedral and poikiloblastic (Figure 6f). Mn concentration gradually decreases from core to near rim where a narrow (70 μm) resorption rind is present (Figure 6f and Table 2). A combination of near-rim compositions and average matrix

Table 2. Compositional Data (in wt %) Used for Near-Garnet-Rim Thermobarometric Analyses[a]

	Garnet Near Rim	Biotite	Plagioclase	Muscovite
LP09-09		(22)	(23)	(28)
SiO_2	37.02	35.55	64.06	45.38
TiO_2	0	1.52	0	0.38
Al_2O_3	21.13	19.35	22.12	35.32
FeO	33.80	18.38	0.09	1.91
MnO	3.18	0.09	0	0.01
MgO	3.27	10.75	0	0.56
CaO	1.49	0.01	3.16	0.01
Na_2O	0.01	0.32	9.63	1.61
K_2O	0	8.87	0.08	8.33
Σ	99.92	98.80	99.14	97.95
LP09-49		(10)	(24)	(8)
SiO_2	36.97	34.98	63.55	45.59
TiO_2	0.08	1.50	0	0.30
Al_2O_3	20.92	18.87	22.58	36.26
FeO	31.65	19.53	0.21	1.42
MnO	7.92	0.15	0	0.03
MgO	2.07	9.30	0	0.67
CaO	1.39	0.01	3.62	0.01
Na_2O	0.02	0.17	9.48	0.99
K_2O	0	9.14	0.09	9.63
Σ	101.06	97.51	99.52	99.41
LP09-02		(9)	(24)	(19)
SiO_2	37.66	36.07	61.59	46.10
TiO_2	0.02	1.72	0	0.52
Al_2O_3	21.25	19.34	24.47	34.86
FeO	32.17	17.93	0.16	1.78
MnO	2.34	0.09	0	0.01
MgO	2.60	10.96	0	1.10
CaO	5.00	0.06	6.19	0.03
Na_2O	0.03	0.20	7.94	0.94
K_2O	0	8.94	0.08	9.40
Σ	101.04	99.30	100.4	99.22
LP09-147gnt1		(44)	—	—
SiO_2	36.67	35.92	—	—
TiO_2	0.28	1.62	—	—
Al_2O_3	20.72	17.88	—	—
FeO	28.86	17.75	—	—
MnO	7.00	0.20	—	—
MgO	2.11	11.35	—	—
CaO	3.73	0.05	—	—
Na_2O	0.03	0.08	—	—
K_2O	0	9.24	—	—
Σ	99.40	98.01	—	—
LP09-147gnt2		(44)		
SiO_2	36.94	35.92	—	—
TiO_2	0.06	1.62	—	—
Al_2O_3	20.78	17.88	—	—
FeO	28.37	17.75	—	—
MnO	6.70	0.20	—	—
MgO	2.18	11.35	—	—
CaO	4.65	0.05	—	—
Na_2O	0.01	0.08	—	—
K_2O	0	9.24	—	—
Σ	99.69	98.01	—	—

[a]Numbers in parentheses represent the number of data points averaged.

Table 3. Compositional Data (in wt %) Used for Garnet Inclusion Thermobarometric Analyses[a]

	Garnet	Biotite	Ilmenite
LP09-09 box 1			
SiO_2	27.26	—	0.02
TiO_2	0.04	—	49.29
Al_2O_3	20.98	—	0
FeO	32.94	—	48.58
MnO	3.93	—	0.80
MgO	3.18	—	0.57
CaO	2.20	—	0.03
Na_2O	0.02	—	0
K_2O	0	—	0
Σ	100.49	—	99.29
LP09-09 box 2			
SiO_2	37.22	—	0.05
TiO_2	0.03	—	49.14
Al_2O_3	20.94	—	0.01
FeO	32.93	—	48.36
MnO	3.79	—	0.63
MgO	3.09	—	0.62
CaO	2.39	—	0.05
Na_2O	0.02	—	0
K_2O	0	—	0
Σ	100.45	—	98.85
LP09-02 box 3			
SiO_2	37.09	36.80	—
TiO_2	0.06	1.50	—
Al_2O_3	21.01	20.11	—
FeO	30.37	18.00	—
MnO	4.20	0.13	—
MgO	2.16	11.22	—
CaO	5.48	0.05	—
Na_2O	0.02	0.17	—
K_2O	0	8.95	—
Σ	100.38	101.00	—
LP09-147 gnt1 box 4			
SiO_2	36.61	—	0.02
TiO_2	0.18	—	50.94
Al_2O_3	20.66	—	0.02
FeO	25.56	—	44.33
MnO	11.64	—	3.12
MgO	1.63	—	0.41
CaO	3.55	—	0.09
Na_2O	0.01	—	0
K_2O	0	—	0
Σ	99.84	—	98.93

[a]Boxes refer to the inclusion location boxes in Figures 6 and 8.

compositions yields a *P-T* estimate of 571 ± 92°C and 7.8 ± 1.4 kbar (Table 1). Inclusions of biotite and core compositions of garnet (Table 3) yield a temperature estimate of 541 ± 25°C (Figure 6f, box 3, and Table 1). The temperature estimate from inclusions is inferred to record prograde metamorphic growth.

LP09-49 was collected from closer to the staurolite zone that is exposed ~5 km to the NE, representing a structurally lower position in the garnet zone of the Haimanta Group (Figure 1b). The sample contains subhedral to anhedral porphyroblasts of garnet in a foliated matrix consisting of biotite, muscovite, quartz, albite, k-feldspar, muscovite, and ilmenite. Garnet porphyroblasts contain quartz, apatite, and small ilmenite inclusions. Garnet porphyroblasts preserve a decrease in Mn content from the interior to the near rim, which is interpreted as growth zoning (Figure 8a and Table 2). A ~20 μm rim of increased Mn content is attributed to a subsequent thermal event that resulted in net transfer reactions [*Kohn and Spear*, 2000]. Using the near-rim composition and averaged matrix compositions of biotite, white mica, and plagioclase yields a *P-T* estimate of 499 ± 99°C and 4.5 ± 1.4 kbar (Figure 8a and Table 1). Small, rare monazite grains occur throughout the matrix.
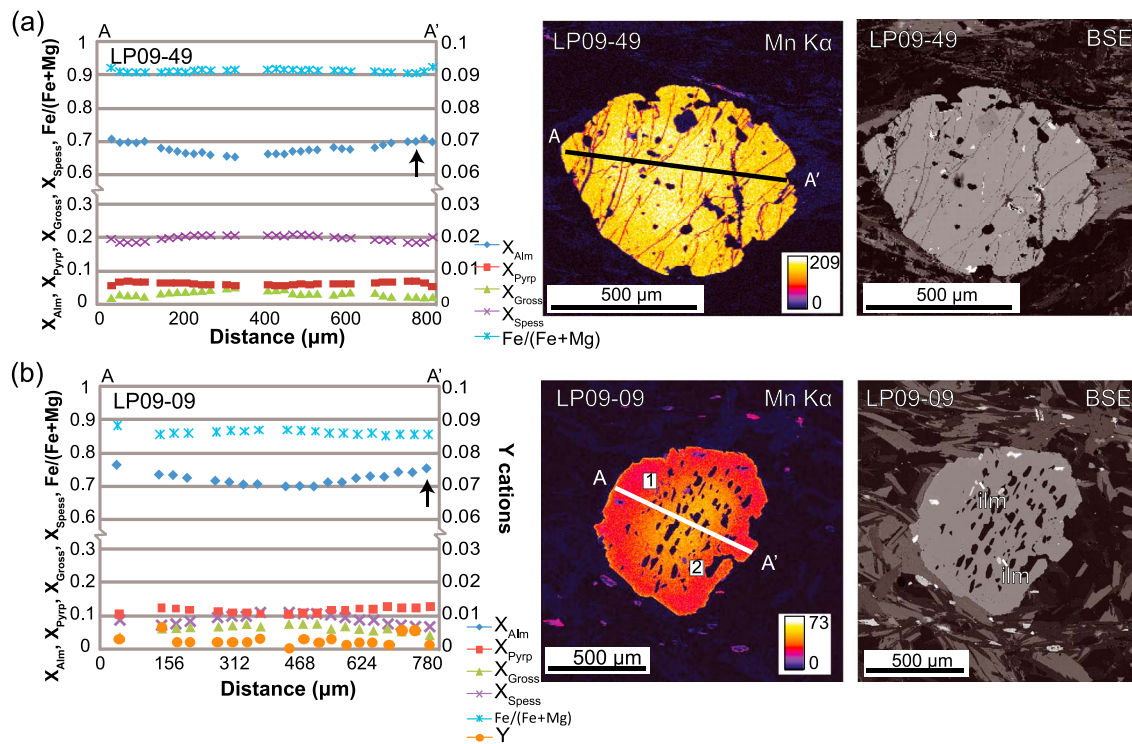
Figure 8. Compositional maps and analytical transects of representative garnet porphyroblasts. (a) LP09-49 is from a ridge above the Spiti and Sutlej Rivers that represents a structurally lower position of the garnet zone than LP09-147. (b) LP09-09 was collected from within the staurolite zone and represents the *P-T* conditions as recorded at positions closest to the dome.

8.2. Staurolite Zone

A garnet-bearing schist LP09-09, with staurolite in the same outcrop (LP09-10) [see *Langille et al.*, 2012], is representative of the metamorphic conditions reached within the staurolite zone (Figure 1b). Aligned inclusions of quartz are concentrated in the interior of the garnet porphyroblasts (Figure 8b). Mn composition in garnet porphyroblasts decreases from the core to near rim where a ~150 μm thick rind of higher Mn occurs (Figure 8b and Table 2). The central portion of the garnet porphyroblast, where aligned inclusions are concentrated, preserves a decrease in Mn concentration from core to near rim that is interpreted as growth zoning. The elevated zone of Mn is attributed to net transfer reactions [*Kohn and Spear*, 2000] and the development of a resorption rind (Figure 8b and Table 2). Using the near-rim composition yielded a *P-T* estimate of 567 ± 105°C and 6.7 ± 1.6 kbar (Tables 1 and 2). Inclusions of ilmenite from two areas near the inner rim yield temperature estimates of 549 ± 26°C and 484 ± 27°C (Figure 8b, boxes 1 and 2, and Tables 1 and 3).

9. Discussion

9.1. Metamorphic Field Gradients

Within the central portion (Figures 1c and 9) of the transect, isolated from the subsequent effects of exhumation along the SD and LPSZ, the Haimanta Group preserves Barrovian metamorphism (D2) [*Chambers et al.*, 2009; *Langille et al.*, 2012, 2014]. Above the SD (Figure 9), a right way-up sequence from the kyanite-staurolite zone to the biotite zone dips NE, defining the metamorphic field gradient (Figures 1d and 2a–2c) [*Chambers et al.*, 2009]. A NW trending F3 synform (Figures 1b–1d), cored by rocks within the biotite zone, creates a region of SW dipping S2 (Figures 2d–2g). On the SW dipping limb of the F3 synform, a metamorphic field gradient increases from the garnet zone (571 ± 92°C and 7.8 ± 1.4 kbar; 499 ± 99°C and 4.5 ± 1.4 kbar) through the staurolite-kyanite zone (567 ± 105°C and 6.7 ± 1.6 kbar) to the cordierite-sillimanite zone. The relationship between metamorphic zones and S2 indicates that the isograds were folded by F3.

We interpret the biotite to staurolite-kyanite zones to record prograde metamorphism during crustal thickening. This timing of maximum burial of the Haimanta Group in the hanging wall of the SD was 30 Ma
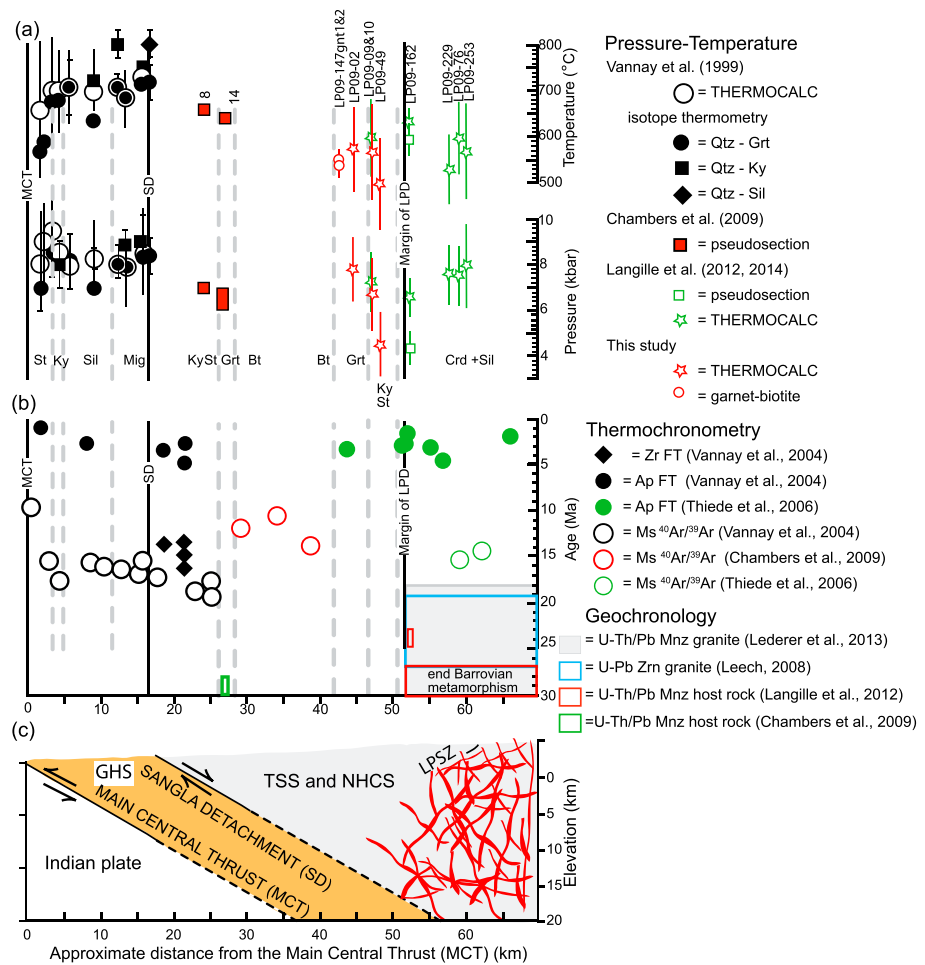
Figure 9. Synthesis of data from the Main Central thrust (MCT) to the Leo Pargil shear zone (LPSZ). (a) *P-T* estimates from the MCT to hanging wall of the Sangla detachment (SD) [*Vannay et al.*, 1999; *Chambers et al.*, 2009], the biotite to the kyanite zones of this investigation, and the Sutlej-Spiti confluence to Leo Pargil dome [*Langille et al.*, 2012, 2014].
(b) Thermochronometry [*Vannay et al.*, 2004; *Thiede et al.*, 2006; *Chambers et al.*, 2009] and geochronology [*Leech*, 2008; *Chambers et al.*, 2009; *Langille et al.*, 2012; *Lederer et al.*, 2013] for the entire transect are included. Leucogranite sample (AW 9-24-04 4) from the LPD [*Webb et al.*, 2011] was excluded because the age (50.4 ± 2.40) represented inherited zircon.
(c) General structures and rock types shown in cross section are adapted from previous work [*Vannay et al.*, 2004]. Cross-section line used to project data is shown as dashed line in Figure 1b and differs from that used in Figure 1c. Vertical gray dashed lines are the approximate boundaries of the metamorphic zones.

[*Chambers et al.*, 2009]. Barrovian metamorphism near the LPD ceased at 29–27 Ma [*Langille et al.*, 2012]. Aside from biotite replacement by chlorite in some samples, the garnet to staurolite-kyanite zones contain assemblages with little evidence for retrograde reactions.

The sillimanite-cordierite zone contains overgrowths on staurolite (LP09-143) and kyanite porphyroblasts [*Langille et al.*, 2012]. Cordierite overgrowths on staurolite represent a disequilibrium texture that records near-isothermal decompression [*Langille et al.*, 2012]. Samples from this portion of the zone contain assemblages that record prograde metamorphism (530–630°C and 7–8 kbar) that were overprinted by synkinematic sillimanite-cordierite during decompression to ~4.5 kbar at >23 Ma [*Langille et al.*, 2012].

Thermobarometric data from this investigation documented relatively isothermal conditions for the suite of samples from which the estimates were derived. The biotite to the staurolite-kyanite zones define a Barrovian sequence that increased in metamorphic grade toward structurally deeper positions. Near the margin of the LPD, these assemblages were overprinted by cordierite and sillimanite during near-isothermal decompression. The resulting metamorphic field gradient is a consequence of two different metamorphic stages.
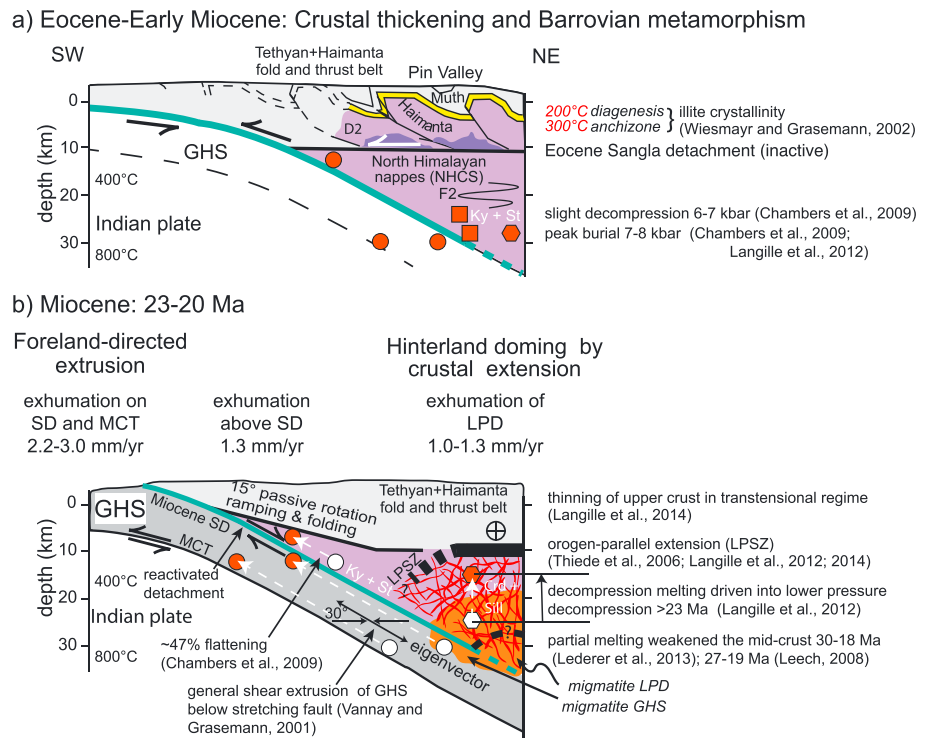
Figure 10. Model for the Sutlej Valley, NW India is after *Vannay et al.* [2004] and *Wiesmayr and Grasemann* [2002]. Schematic Indian plate and Greater Himalayan Series (GHS) are modified from *Vannay et al.* [2004]. (a) Interpretation of the Haimanta Group, Tethyan Sedimentary Series (TSS), the North Himalayan nappes, and the North Himalaya Crystalline Series (NHCS) that formed above the Indian plate during the Eocene-Miocene. Placement of the Sangla detachment depicts the Eocene position. Geology from Pin Valley is after *Wiesmayr and Grasemann* [2002]. (b) Subsequent evolution of the region during the Miocene. Exhumation rates and pressure-temperature estimates are from *Chambers et al.* [2009] and *Langille et al.* [2012]. Ages of leucogranites are from *Leech* [2008] and *Lederer et al.* [2013]. Black lines bracket the upper and lower positions of the LPSZ. Eigenvectors for general shear extrusion model are after *Vannay and Grasemann* [2001]. Representative samples from the GHS [*Vannay et al.*, 2004], the LPD [*Langille et al.*, 2012], and the North Himalaya Crystalline Series (NHCS) [*Vannay et al.*, 2004; *Chambers et al.*, 2009] are included: polygons, *Langille et al.* [2012]; squares, *Chambers et al.* [2009]; circles, *Vannay et al.* [2004].

9.2. Strain Gradients

Systematic collection of mesoscale structural data (*n* = 1445) from the hanging wall of SD to the southern edge of the LPD enabled this investigation to test for structural/strain changes when approaching the dome (Figure 1d). These data are relatively consistent for ~25 km between Domain 1 and Domain 3. The majority of the transect is characterized by an early phase (D2) of tight to isoclinal, NW trending, shallowly plunging F2 folds that thickened the Haimanta Group, resulting in Barrovian metamorphism. These F2 and S2 fabrics, along with metamorphic zones, where subsequently folded by upright, open F3 folds.

Beginning ~ 2 km south of the Spiti/Sutlej confluence, NW trending F2 folds were rotated to an E-W trending orientation, coinciding with the margin of the injection complex and the cordierite-sillimanite zone. Several possibilities could describe this transition within Domain 4. In one scenario, the north dipping S1/S2 might be on the northern limb of an F3 fold. Alternatively, the emplacement and/or exhumation of the LPD could have rotated the NW trending F2 folds, dominant in Domains 1–3, to an E-W orientation in Domain 4. The LPSZ, exposed at structurally higher levels near the village of Nako (Figure 1b), is a west dipping, high-temperature shear zone (>650°C to 280°C) with a downdip stretching lineation [*Langille et al.*, 2014]. Perhaps the confluence area near Domain 4 represents the transition between Domains 1–3 and the rotation of F2 fold hinges into parallelism with the stretching lineation of the LPSZ near the villages of Leo and Nako [*Langille et al.*, 2014]. *Hintersberger et al.* [2011] proposed that these shear zone fabrics were part of D4 arc-parallel extension [*Langille et al.*, 2014].

Microstructures and mineral assemblages record a transition, over ~12 km horizontal distance, between rocks that are near the biotite zone (Figure 6c) to those within the cordierite-sillimanite zone on the margin of the injection complex (Figure 7f). This transition records two phases of metamorphism, involving Barrovian

metamorphism followed by near-isothermal decompression [*Langille et al.*, 2012]. D2 crenulation cleavage is the dominant foliation within the garnet zone (Figure 7b). Staurolite and kyanite porphyroblasts overgrew F2 crenulations, indicating that they postdated the majority of D2 deformation (Figures 7a, 7d, and 7e). These suggest that progressive D2 deformation occurred during progressive Barrovian metamorphism. This is compatible with microstructural evidence from the southwestern exposures of the Haimanta Group in the hanging wall of the SD [*Chambers et al.*, 2009]. Near the margin of the dome, cordierite and sillimanite overgrowths occur on kyanite and staurolite (Figure 7f). Between biotite and cordierite zones the crenulation cleavage is maintained, but some rotation of porphyroblasts occurred. Microstructures are dominated by 120° triple junctions of quartz grain boundaries, which indicate some component of annealing through a process such as grain boundary area reduction [*Passchier* and *Trouw*, 2005]. Grain boundary area reduction probably continued after deformation, suggesting that the temperatures were adequate for static recrystallization.

9.3. Summary of Strain and Metamorphic Field Gradients

Mesoscale and microscale structures, metamorphic porphyroblasts, compositional zoning in garnet porphyroblasts, and an injection complex define a gradient into the southern margin of LPD, beginning ~2 km south of the confluence of the Spiti and Sutlej Rivers. Following Barrovian metamorphism, a ductile shear zone, within the Haimanta Group and at structurally higher positions (e.g., Shian, Pin, and Muth Formations; Figure 1b) on the southwestern margin of the LPD, formed to accommodate exhumation at >23 Ma [*Hintersberger et al.*, 2011; *Langille et al.*, 2012, 2014]. Exhumation continued through the ^{40}Ar/^{39}Ar closure temperature of white mica (~350°C) at ~16 Ma [*Thiede et al.*, 2006; *Langille et al.*, 2012]. D4 shear fabrics overprinted garnet, staurolite, and kyanite porphyroblasts during top west (255) extension [*Langille et al.*, 2012]. D4 occurred during arc-parallel extension [*Hintersberger et al.*, 2011]. Data from this investigation did not locate an equivalent zone of mylonitic rocks between the biotite zone and injection complex on the southern margin of the LPD. We propose that the area near the confluence represents a deeper structural position within the southern margin of the dome where D2 deformation is more distributed than in the LPSZ exposed near Nako (Figure 1b).

9.4. Proposed Conceptual Tectonic Models

To tie the evolution of the lithotectonic units in Sutlej Valley and the LPD into the regional context, we modify Figure 11 of *Vannay et al.* [2004] and Figure 8 of *Wiesmayr and Grasemann* [2002] to create a schematic model, exploring the interplay between crustal thickening, Barrovian metamorphism, partial melting, and exhumation (Figure 10). Because extensive data sets are available, models and interpretations of the cross sections of the Sutlej Valley [*Vannay et al.*, 1999, 2004; *Vannay and Grasemann*, 2001; *Chambers et al.*, 2009] and Pin Valley to the NW [*Wiesmayr and Grasemann*, 2002] create a framework for our proposed modifications of the northern portion to build snapshots of (1) Eohimalayan phase (Eocene-early Miocene) of crustal thickening and Barrovian metamorphism and (2) Neohimalayan phase (Miocene) of near-isothermal decompression for the LPD beginning at >23 Ma that corresponds to extrusion of the GHS.

9.4.1. Eohimalayan (Eocene-Early Miocene)

A cross section (Figure 10a) for the Tethyan + Haimanta fold and thrust belt from the Pin-Lingti Valleys represents the conditions of the Eocene SD prior to Miocene rotation due to synclinal bending [*Wiesmayr and Grasemann*, 2002; *Neumayer et al.*, 2004] and includes (1) structural geometry and thicknesses of the rock units, (2) 10 km depth of the Eocene SD using restoration of the Tethyan + Haimanta fold and thrust belt, and (3) paleotemperature estimates and ^{40}Ar/^{39}Ar ages from illite that grew parallel to the axial surface of F2 folds at 45 Ma [*Wiesmayr and Grasemann*, 2002]. Assuming that these conditions represent the general characteristics of the upper crust during the Eocene-Oligocene, they are schematically projected SE to explore their relationship with deeper structural positions that are provided by exposures of the Haimanta Group in Sutlej Valley, which are the focus of this investigation. The cross section for the northern portion is taken directly from Pin-Lingti Valley [*Wiesmayr and Grasemann*, 2002; *Neumayer et al.*, 2004], yet those projected to the SW are schematic and intended to show the possible structural depth and the style of deformation at these depths. The lowest units of the fold and thrust belt are the Haimanta Group with Paleozoic Kinnaur Kailas granite. *Wiesmayr and Grasemann* [2002] proposed that this subhorizontal detachment accommodated underthrusting of the GHS and NHCS. This model represents the conditions after the Tethyan + Haimanta fold and thrust belt and NHCS were tectonically juxtaposed along the Eocene SD [*Wiesmayr and Grasemann*, 2002; *Vannay et al.*, 2004]. The dip of the subduction interface (green line, Figure 10a) of the Indian plate (e.g., future GHS bounded by the MCT and SD) was 30° [*Vannay and Grasemann*, 2001].

P-T-t data from the Haimanta Group in the Sutlej River, located in the modern hanging wall of the SD, indicates that these rocks reached ~515°C and 7–8 kbar at >34–28 Ma with peak burial at 30 Ma. This was followed by slight decompression to 640–660°C and 6–7 kbar [*Chambers et al.*, 2009]. Rocks that became part of the LPD, the Haimanta Group, reached ~530–630°C and ~7–8 kbar during Barrovian metamorphism that ended by 29–27 Ma [*Langille et al.*, 2012]. An average lithostatic pressure gradient (3.7 km/kbar) was used to estimate a minimum structural depth (26–30 km) of the Haimanta Group. Although the current exposures are an artifact of several phases of deformation that occurred after crustal thickening (D1–D3), these depth estimates are consistent with the *P-T* conditions that the upper structural positions of the GHS exposed in Zanskar (660–720°C; 8–10 kbar) reached at 33 Ma [*Vance and Harris*, 1999; *Dèzes et al.*, 1999] and the North Himalayan nappes reached (~600–700°C; ~8–8.5 kbar) at 37–36 Ma [*Stübner et al.*, 2014]. The composite model cross section combined data from the fold and thrust belt at 45 Ma, the Eocene SD, and average depth of porphyroblast growth (30–27 Ma). Representative samples from the GHS [*Vannay et al.*, 2004], LPD [*Langille et al.*, 2014], and NHCS [*Vannay et al.*, 2004; *Chambers et al.*, 2009] are included (Figure 10a).

9.4.2. Neohimalayan (Early Miocene)

The second stage (Figure 10b) builds on the final conditions of the first (Eohimalayan) to demonstrate the relationship between early Barrovian metamorphism (30–27 Ma) and subsequent exhumation of the GHS and LPD by coeval movement on the Miocene SD and LPSZ at ~23 Ma [*Wiesmayr and Grasemann*, 2002; *Vannay et al.*, 2004; *Langille et al.*, 2012]. The Eocene SD is shown at the base of the Tethyan + Haimanta fold and thrust belt. The SW portion of the Eocene SD, along with the Tethyan + Haimanta fold and thrust belt in the hanging wall, underwent a 15° passive rotation toward the NE [*Wiesmayr and Grasemann*, 2002]. The approximate upper contact of LPSZ is shown in Figure 10b as a black line. A dashed black line in the zone of partial melting represents the approximate lower limit of the rock that the LPSZ eventually juxtaposed. The upper structural position of the LPSZ is similar to that of the Eocene SD [*Wiesmayr and Grasemann*, 2002]. During this period of the ductile deformation, the LPSZ extended from structurally higher positions of the TSS (e.g., Shian, Pin, and Muth Formations) to the deeper structural positions within the Haimanta Group of the NHCS. This portrayal is schematic because at the end of its ductile deformation the LPSZ juxtaposed migmatite in the core with the TSS above [*Langille et al.*, 2014]. The average depth of Barrovian metamorphism (26–30 km) defined the starting conditions for near-isothermal decompression (~4 kbar; depth of ~15 km) at >23 Ma [*Langille et al.*, 2012]. Partial melting, which occurred at deeper structural positions within the GHS (see section 9.7), fed the injection complex from 30 to 18 Ma [*Lederer et al.*, 2013]. An injection complex within the Haimanta Group and a potential site of partial melt (yielding leucogranitic magma) within a deeper structural position of the GHS and/or NHCS [*Lederer et al.*, 2013] is shown in orange. Following peak metamorphism, metamorphic field gradients in the Haimanta Group, located in the hanging wall of the SD, were vertically thinned by ~47% during south directed extrusion of the GHS [*Chambers et al.*, 2009]. Exhumation rates for the GHS and the hanging wall of the SD were 2.2–3.0 mm/yr and 1.3 mm/yr, respectively [*Chambers et al.*, 2009]. The LPD was exhumed at a minimum rate of ~1.3 mm/yr (29–23 Ma) [*Langille et al.*, 2012]. To convey generalized particle paths, new positions for the representative samples from the GHS [*Vannay et al.*, 2004], LPD [*Langille et al.*, 2014], and NHCS [*Vannay et al.*, 2004; *Chambers et al.*, 2009] were added (Figure 10b).

9.5. Crustal Thickening and Shear Zone Localization

Crustal thickening above the Eocene SD created the Tethyan + Haimanta fold and thrust belt that culminated in the formation of south vergent folds and thrust faults at ~45 Ma (Figure 10a) [*Wiesmayr and Grasemann*, 2002; *Neumayer et al.*, 2004]. Buckling of sedimentary rocks created an S2 axial plane cleavage at anchizonal to epizonal metamorphic temperatures [*Wiesmayr and Grasemann*, 2002; *Neumayer et al.*, 2004]. Beneath the Eocene SD, penetrative fabric development during the formation of F2 folds, as defined by this investigation, culminated with the cessation of Barrovian metamorphism in the midcrust by ~30 Ma [*Chambers et al.*, 2009; *Langille et al.*, 2012]. Using an approximate restoration of the upright F3 folds, it is possible to visualize the geometry of F2 folds as they formed (Figure 4a). The isoclinal F2 folds would be close to recumbent (Figures 1c, 3a, and 10a). The Eocene SD separated the brittle upper crust (Tethyan + Haimanta fold and thrust belt) above from the ductile midcrustal rocks (e.g., GHS or NHCS) below [*Wiesmayr and Grasemann*, 2002; *Vannay et al.*, 2004]. An upper crust dominated by brittle deformation and upright folds can also be described as an orogenic superstructure, while ductile rocks with subhorizontal folds located structurally below a shear zone or detachment are orogenic infrastructures [*Culshaw et al.*, 2006]. One assumption of the model is that the subhorizontal structures overprinted earlier upright structures [*Culshaw et al.*, 2006]. Although some

terminology of orogenic superstructure and infrastructure are appropriate for these conceptual models, data from this investigation demonstrated that the upright F3 folds overprinted the early D2 recumbent fabrics. In addition to the Himalaya, orogenic superstructures and infrastructures have been applied to many different orogens [e.g., *Jamieson and Beaumont*, 2013].

The timing of Barrovian (Eohimalayan) metamorphism in the Haimanta Group from Sutlej Valley (~30 Ma) and the depth of burial (26–30 km) are similar to the upper portions of the GHS near the sillimanite and the kyanite zones (i.e., Zanskar) as well as the North Himalayan nappes [*Stübner et al.*, 2014]. Following the logic of *Stübner et al.* [2014], we propose that folds and Barrovian metamorphism, within the Haimanta Group of this transect, developed in response to crustal shortening and thickening during the Eohimalayan phase as part of the North Himalayan nappes (Figure 10a).

9.6. Depth of Burial

The depth for Barrovian metamorphism (26–30 km), within the Haimanta Group of the North Himalayan nappes, suggests that folds developed in the Haimanta Group at deeper structural positions than the Eocene SD (Figure 10a) as projected to 10 km using the Tethyan + Haimanta fold and thrust belt in Pin Valley [*Wiesmayr and Grasemann*, 2002]. Temperature estimates, derived from illite crystallinity (200–300°C) in the Tethyan + Haimanta fold and thrust belt exposed in Pin Valley, indicate that deformation at 7–10 km culminated at ~45 Ma [*Wiesmayr and Grasemann*, 2002]. At this time, underthrusting of the Indian plate along the SD resulted in crustal thickening and metamorphism in the GHS and NHCS [*Wiesmayr and Grasemann*, 2002]. Rocks located between the Eocene SD and the underthrusting Indian plate reached ~600°C and 7–8 kbar (26–30 km), with maximum burial at 30 Ma [*Chambers et al.*, 2009; *Langille et al.*, 2012].

Garnet growth during prograde metamorphism involved heating (from 550–570°C to 660–700°C) in the Zanskar nappes (33–28 Ma) within 5–10 Ma of burial [*Vance and Mahar*, 1998; *Vance and Harris*, 1999]. In samples from Zanskar, thermal reequilibration following burial implies that the shortening structures (thrusts) were between 10 and 15 km above the samples [*Vance and Mahar*, 1998; *Vance and Harris*, 1999]. Our proposed model cross section for the Eohimalayan phase of metamorphism and deformation reveals that the ~20 km difference between structural positions of the Eocene SD at the base of the Tethyan + Haimanta fold and thrust belt and the base of the North Himalayan nappes above the subducting Indian plate is of similar range to those documented in Zanskar. As predicted by *Vance and Harris* [1999], movement on the Eocene SD to the Tethyan + Haimanta fold and thrust belt during crustal thickening in the Pin Valley at 45 Ma could have buried the deepest positions of the North Himalayan nappes, as exposed in this transect, to 26–30 km, followed by thermal reequilibration and the end of Barrovian metamorphism at 30–27 Ma [*Chambers et al.*, 2009; *Langille et al.*, 2012].

9.7. Depth and Source Region of Partial Melting

The maximum depth of burial in the Haimanta Group of the North Himalayan nappes can be used as a starting point for exploring relationships between *P-T-t* paths and their control on crustal melting [*Harris and Massey*, 1994; *Harris et al.*, 1995; *Patiño Douce and Harris*, 1998]. During crustal thickening, rocks in the study area experienced Barrovian metamorphism in the GHS (600–750°C; 8 kbar) and the North Himalayan nappes (650–700°C; 6–8 kbar) at ~30 Ma [*Vannay et al.*, 2004; *Chambers et al.*, 2009; *Langille et al.*, 2012]. These depths are equivalent to midcrustal structural positions of the GHS in the footwall of the Zanskar shear zone [*Vance and Harris*, 1999; *Dèzes et al.*, 1999] as well as the North Himalayan nappes [*Stübner et al.*, 2014]. Rocks exposed within the LPSZ record maximum temperatures of ~600–650°C, with likely higher temperatures in the migmatitic core [*Langille et al.*, 2012, 2014]. Wet melting is predicted to occur between 750 and 800°C at 8 kbar [*Patiño Douce and Harris*, 1998]. It is reasonable to assume that melt generation that fed the injection complex within the dome came from deeper structural levels, potentially within the migmatitic core or deeper. The generalized model (Figure 10b) indicates that the GHS [*Vannay et al.*, 2004] and the base of the North Himalayan nappes were located at greater depths than the maximum depth recorded by samples in the LPD [*Langille et al.*, 2012]. Therefore, these areas are capable of partial melting [*Patiño Douce and Harris*, 1998; *Vance and Harris*, 1999; *Lederer et al.*, 2013]. The period of semicontinuous partial melting of the GHS (30–18 Ma) was initiated by decompression that caused muscovite dehydration reactions between 30 and 23 Ma [*Lederer et al.*, 2013]. The onset of near-isothermal decompression at >23 Ma [*Langille et al.*, 2012], driven by extension, resulted in the formation of the extensive injection complex in the LPD and continued until 18 Ma [*Lederer et al.*, 2013]. Decompression

should enhance melt production by movement through the fluid-absent incongruent breakdown of muscovite as documented for similar structural positions in Zanskar [*Vance and Harris*, 1999]. For Zanskar, *Steck* [2003] proposed that heating resulted in partial melting of the GHS. In some areas of NW India, located between the Zanskar shear zone and this transect, extrusion did not involve significant melting [*Stübner et al.*, 2014].

Partial melting weakens the midcrust [*Cruden*, 1990]. In channel flow models, the relatively weak layer of partial melting in the midcrust is driven laterally by gradients in lithostatic pressure [*Beaumont et al.*, 2001; *Grujic et al.*, 2002; *Godin et al.*, 2006]. When applied to the Himalaya-Tibet system, the weakened portion of the GHS is extruded southward between the STDS above and MCT below [*Beaumont et al.*, 2001]. These thermomechanical models include two main types of dome-forming mechanisms [*Beaumont et al.*, 2001, 2004]: (1) hinterland doming by crustal extension and (2) doming triggered by underthrusting. Hinterland doming invokes thinning of the crust due to a zone of localized extension, resulting in additional crustal thinning and channel exhumation [*Beaumont et al.*, 2004]. This scenario arises when the timescale of channel flow into the region of extension exceeds the timescale of thinning [*Beaumont et al.*, 2004]. During thinning, zones of partial melt are driven into areas of relatively lower pressure [*Beaumont et al.*, 2004]. Doming triggered by underthrusting results from a frontal ramp that cuts into the midcrustal channel, resulting in exhumation of the channel into the upper crust as a dome above the ramp [*Beaumont et al.*, 2004]. Domes triggered by underthrusting can be translated toward the foreland [*Beaumont et al.*, 2004].

Because of the overlap in timing between the period of partial melting, near-isothermal decompression, and high-temperature top west deformation of the LPSZ, *Langille et al.* [2012] proposed that a modified version of hinterland doming was the more appropriate model for the LPD. Hinterland doming by crustal extension [*Beaumont et al.*, 2004] could be applicable to the LPD because of its location within a region of oblique convergence, which created a zone of transtension across the Karakoram fault between the Tibetan plateau and NW India [*Hintersberger et al.*, 2010, 2011; *Langille et al.*, 2012, 2014]. Hinterland doming by crustal extension creates a localized area of exhumation to the north [*Beaumont et al.*, 2004]. Prior to exhumation, rocks of the LPD were deep within the North Himalayan nappes (650–700°C; 6–8 kbar). *P-T* data from the GHS (750°C; 8 kbar) indicate that it reached slightly deeper structural positions [*Vannay and Grasemann*, 2001]. The position is consistent with the *P-T* conditions for the GHS where partial melting was possible before the onset of doming [*Lederer et al.*, 2013]. Beginning at >23 Ma, the LPD experienced orogen-parallel extension in the hinterland [*Langille et al.*, 2012, 2014]. Decompression by displacement on the LPSZ was active at ~20 Ma [*Lederer et al.*, 2013]. As proposed by *Langille et al.* [2012, 2014], thinning of the crust above this zone of partial melting, below the base of the North Himalayan nappes, drove decompression and partial melting during doming and orogen-parallel extension. Moderate partial melting was localized at the top of the GHS [*Vannay et al.*, 2004], while more extensive partial melting weakened the midcrust below the current exposure of the LPD during orogen-parallel extension [*Langille et al.*, 2012, 2014]. Although this model uses the concept of hinterland doming by crustal extension to drive doming [*Beaumont et al.*, 2004], the source of partial melt was derived from muscovite dehydration within the GHS below the North Himalayan nappes instead of from beneath the Tibetan plateau. *Steck* [2003] proposed this distinction between partial melt that was derived from the base of the thickened crust and midcrustal flow from beneath the Tibetan plateau.

9.8. Exhumation of Midcrustal Rocks

Initiation of movement on the MCT (23 Ma) caused top-to-the-northeast extension within mylonites of the SD and overprinting of earlier, south directed fabrics that were related to thrusting at the base of the Haimanta Group or perhaps the North Himalayan nappes [*Vannay and Grasemann*, 2001; *Vannay et al.*, 2004]. The paired MCT-SD system continued to exhume the GHS between 23 and 16 Ma [*Vannay et al.*, 2004]. *Chambers et al.* [2009] proposed that during this time interval the GHS experienced a significantly faster exhumation rate (~2.2 to 3.0 mm year^{-1}) than the TSS (1.3 mm yr^{-1}), implying that the TSS (e.g., the Haimanta Group and overlying TSS) was decoupled from the extruding GHS by 23 Ma (Figures 9 and 10b). ^{40}Ar/^{39}Ar white mica ages for the entire transect revealed that displacement on the SD ended prior to exhumation through ~350°C. By ~ 20–15 Ma, this system was locked in below the brittle-ductile transition zone. At the current level of exposure, the SD did not propagate as a brittle fault in the upper crust.

Detailed kinematic analysis and the distribution of isograds in Sutlej Valley were the foundation for extrusion models of the GHS [*Grasemann et al.*, 1999; *Vannay and Grasemann*, 2001]. *Vannay and Grasemann* [2001] provide a detailed discussion regarding the validity of general shear extrusion versus channel flow and other

models. Because a general shear extrusion model was already established for the GHS in Sutlej Valley, it is incorporated into this model for the LPD. Quantitative kinematic analysis from the MCT defined an early stage of simple shear on the margins that was followed by a higher contribution of pure shear in the core of a tapered wedge [*Grasemann et al.*, 1999]. The distribution of isograds and near-isobaric (8 kbar) conditions across the GHS resulted in a model of general shear extrusion of the GHS between the SD and MCT [*Vannay and Grasemann*, 2001]. Because the isobaric samples were exhumed from peak burial without rotation, they were interpreted to record the shortening eigenvector [*Vannay and Grasemann*, 2001]. The stretching eigenvector was parallel to the boundaries of the shear zone (Figure 10b). The cosine of the dip of the SD and MCT (30°) was used to estimate mean kinematic vorticity (W_m) of 0.86 [*Vannay and Grasemann*, 2001]. General shear extrusion resulted in 43% thinning to recreate the 10 km thick GHS [*Vannay and Grasemann*, 2001]. Based on assumptions of the model, the two shear zones merged near an approximate depth of the Main Himalayan thrust (MHT) at 50 km. The MHT would have extended beneath the zone of the LPD activity. During extrusion of the GHS, rocks in the hanging wall were fixed relative to the footwall. The approximate duration for extrusion was 2 Ma [*Vannay and Grasemann*, 2001]. The LPD was located in the hanging wall of the stretching fault during extrusion of the GHS. Decompression during hinterland doming by crustal extension would occur as the GHS experienced general shear extrusion (Figure 10b). The stretching fault would decouple near-isothermal decompression and partial melting of the LPD and extrusion of the GHS while both were active.

During the Miocene, the Eocene SD at the base of the Tethyan + Haimanta fold and thrust belt experienced passive rotation of 15° toward the NE [*Wiesmayr and Grasemann*, 2002]. The projection of the SD, as a horizontal surface to the NE, represented the original geometry of the Eocene SD prior to rotation [*Wiesmayr and Grasemann*, 2002]. At 45 Ma, the horizontal detachment marked the contact between the underthrusting GHS-NHCS below and Tethyan + Haimanta fold and thrust belt above [*Wiesmayr and Grasemann*, 2002]. Extrusion of the GHS did not appear to be decoupled along this shallow-dipping detachment (e.g., Eocene SD) at the base of the Tethyan + Haimanta fold and thrust belt [*Neumayer et al.*, 2004] but instead along the 30° dipping surface of the Miocene SD that defined the base of the NHCS and the top of the GHS [*Vannay and Grasemann*, 2001; *Wiesmayr and Grasemann*, 2002]. This Miocene SD acted as a stretching fault during extrusion of the GHS as part of the general shear extrusion model [*Vannay and Grasemann*, 2001].

Exhumation of the LPD by >23 Ma occurred along the contact between the NHCS and Tethyan + Haimanta fold and thrust belt (Eocene SD). The LPSZ was a >1 km thick shear zone in the Haimanta Group [*Thiede et al.*, 2006; *Langille et al.*, 2014] as well as structurally higher marble and quartzite that are probably the Shian, Muth, and/or Pin Formations [see *Thiede et al.*, 2006]. At deeper structural positions, the LPSZ extended through the Haimanta Group of the North Himalayan nappes and to the zone of partial melting (Figure 10b). Exhumation rates for the LPD, between the end of Barrovian metamorphism at 29 Ma [see *Langille et al.*, 2012] and initiation of decompression and extension at >23 Ma, were 1.3 mm/yr [*Langille et al.*, 2012]. Between 30 and 23 Ma, partial melting of the GHS initiated [*Lederer et al.*, 2013]. Decompression was followed by continued emplacement of the leucogranite injection complex between 23 and 18 Ma [*Lederer et al.*, 2013]. Rapid uplift of rocks resulted in dome formation that caused decompression of partially melted midcrustal rocks. *Langille et al.* [2012, 2014] proposed that the localized dome could be, in part, due to hinterland thinning of the crust within a zone of transtension. The LPSZ occurred at a similar structural level as the horizontal Eocene SD, with Tethyan + Haimanta fold and thrust belt in the hanging wall and the Haimanta Group of the North Himalayan nappes in the footwall (Figure 10b). This implies that during the Miocene, the LPSZ formed within the location of the Eocene SD. Undeformed quartzite from the TSS in the middle of the transect, near Ropa, demonstrates that the southern extent of the LPSZ is limited to the area that coincides with the margin of the LPD and injection complex (Figure 10b).

At different times between the Eocene and the Miocene, deformation was localized along contacts between the Eocene SD and the Miocene SD. These accommodated exhumation in response to the dominant kinematic setting in different portions of the orogen that favored foreland-directed extrusion or orogen-parallel extension in the hinterland. While foreland-directed extrusion has been documented in many other portions of the orogen, orogen-parallel extension in NW India is attributed to more regional processes that were related to the far-field movement on the Karakoram fault [*Thiede et al.*, 2006; *Hintersberger et al.*, 2010, 2011]. These processes are more specific to this portion of the orogen [*Langille et al.*, 2014]. Strain was localized near reactivated crustal anisotropies that formed during crustal thickening (e.g., GHS-NHCS or TSS-NHCS contacts). In this portion of the Himalaya, multiple surfaces could have acted as localized zones for reactivation, including the contact at the base of the Tethyan + Haimanta fold and thrust belt [*Wiesmayr and*

Grasemann, 2002; *Neumayer et al.*, 2004] and the deeper NHCS-GHS contact [*Vannay and Grasemann*, 2001; *Vannay et al.*, 2004]. Additionally, the Eocene SD near the base of the Tethyan + Haimanta fold and thrust belt was reactivated by the LPSZ to accommodate doming of the LPD in the hinterland during orogen-parallel extension ~22 Ma after its initial formation (Figure 10b). The localization of shear zones was controlled by a combination of rheologic contrasts, zones of partial melting, and the kinematic setting for a particular portion of the orogen (e.g., foreland-directed extrusion versus orogen-parallel extension in the hinterland).

10. Conclusions

New mesoscale and microscale structural data were combined with pressure-temperature estimates from the Haimanta Group in the upper Sutlej Valley, NW India, to characterize the relationship between crustal thickening, metamorphism, strain localization, reactivation, and partial melting. Crustal thickening resulted in Barrovian metamorphism that culminated during the Oligocene. Our data define a metamorphic and deformational field gradient that increases from the garnet zone (571 ± 92°C and 7.8 ± 1.4 kbar; 499 ± 99°C and 4.5 ± 1.4 kbar) through the staurolite-kyanite zone (567 ± 105°C and 6.7 ± 1.6 kbar) to the margin of the Leo Pargil dome. Mesoscale structural data record two generations of NW trending folds that are consistent for the majority of the 28 km long transect until the SW margin of the Leo Pargil dome. On the NE margin of the transect, porphyroblasts in the Haimanta Group that grew during Barrovian metamorphism were overprinted by cordierite and sillimanite as decompression occurred on the Leo Pargil shear zone at >23 Ma. When combined with published data from deeper structural positions of the Sutlej Valley, as well as higher structural positions of Pin Valley, new results from this investigation are used to modify a two-stage conceptual tectonic model for the Eocene-Miocene. These models exclude the late Miocene to recent. Rocks located at positions below the horizontal Eocene Sangla detachment at 10 km, which record Barrovian metamorphism, are correlated to the North Himalayan nappes. Partial melting below the North Himalayan nappes, combined with localized orogen-parallel extension in the hinterland, resulted in decompression of the Leo Pargil dome at >23 Ma. The Leo Pargil shear zone, which formed on the reactivated contact (Eocene Sangla detachment) between the Tethyan + Haimanta fold and thrust belt above and North Himalayan Crystalline Series below, accommodated exhumation. As the GHS was extruded between the Main Central thrust and SD 23–16 Ma, the Leo Pargil dome was exhumed at a rate of ~1.3–1.1 mm/yr, injected by leucogranites (30–18 Ma), and exhumed during top-down-to-the-west displacement.

References

Allmendinger, R. W., N. C. Cardozo, and D. Fisher (2013), *Structural Geology Algorithms: Vectors & Tensors*, 289 pp., Cambridge Univ. Press, Cambridge, England.

Aoya, M., S. Wallis, T. Kawakami, J. Lee, Y. Wang, and H. Maeda (2006), The Malashan gneiss dome in south Tibet: Comparative study with the Kangmar dome with special reference to kinematics of deformation and origin of associated granites, in *Channel Flow, Ductile Extrusion and Exhumation in Continental Collision Zones*, edited by R. D. Law, M. P. Searle, and L. Godin, *Geol. Soc. London, Spec. Publ.*, *268*, pp. 471–495.

Beaumont, C., R. A. Jamieson, M. H. Nguyen, and B. Lee (2001), Himalayan tectonics explained by extrusion of a low-viscosity crustal channel coupled to focused surface denudation, *Nature*, *414*, 738–742, doi:10.1038/414738a.

Beaumont, C., R. A. Jamieson, M. H. Nguyen, and S. Medvedev (2004), Crustal channel flows: 1. Numerical models with applications to the tectonics of the Himalayan-Tibetan orogen, *J. Geophys. Res.*, *109*, B06406, doi:10.1029/2003JB002809.

Bettinelli, P., J. P. Avouac, M. Flouzat, F. Jouanne, L. Bollinger, P. Willis, and G. Chitrakar (2006), Plate motion of India and interseismic strain in the Nepal Himalaya from GPS and DORIS measurements, *J. Geod.*, *80*(8), 567–589.

Bilham, R., K. Larson, and J. Freymueller (1997), GPS measurements of present-day convergence across the Nepal Himalaya, *Nature*, *386*, 61–64, doi:10.1038/386061a0.

Burchfiel, B. C., and L. H. Royden (1985), North-south extension within the convergent Himalayan region, *Geology*, *13*, 679–682, doi:10.1130/0091-7613(1985)13<679:NEWTCH>2.0.CO;2.

Burchfiel, B. C., Z. Chen, K. Hodges, Y. Liu, L. H. Royden, C. Deng, and J. Xu (1992), The South Tibetan detachment system, Himalayan orogen: Extension contemporaneous with and parallel to shortening in a collisional mountain belt, *Spec. Pap. Geol. Soc. Am.*, *269*, 1–41, doi:10.1130/SPE269-p1.

Burg, J. P., M. Brunel, D. Gapais, G. M. Chen, and G. H. Liu (1984a), Deformation of leucogranites of the crystalline Main Central Sheet in southern Tibet (China), *J. Struct. Geol.*, *6*, 535–542, doi:10.1016/0191-8141(84)90063-4.

Burg, J. P., M. Guirand, G. M. Chen, and G. C. Li (1984b), Himalayan metamorphism and deformation in the North Himalayan Belt (southern Tibet, China), *Earth Planet. Sci. Lett.*, *69*, 391–400, doi:10.1016/0012-821X(84)90197-3.

Caddick, M. J., M. J. Bickle, N. B. W. Harris, T. J. B. Holland, M. S. A. Horstwood, R. R. Parrish, and T. Ahmad (2007), Burial and exhumation history of a lesser Himalayan schist: Recording the formation of an inverted metamorphic sequence in NW India, *Earth Planet. Sci. Lett.*, *264*, 375–390, doi:10.1016/j.epsl.2007.09.011.

Chambers, J., M. Caddick, T. Argles, M. Horstwood, S. Sherlock, N. Harris, R. Parrish, and T. Ahmad (2009), Empirical constraints on extrusion mechanisms from the upper margin of an exhumed high-grade orogenic core, Sutlej valley, NW India, *Tectonophysics*, *477*, 77–92, doi:10.1016/j.tecto.2008.10.013.

Chambers, J. A., T. W. Argles, M. S. A. Horstwood, N. B. W. Harris, R. R. Parrish, and T. Ahmad (2008), Tectonic implications of Palaeoproterozoic anatexis and late Miocene metamorphism in the Lesser Himalayan Sequence, Sutlej Valley, NW India, *J. Geol. Soc. London*, *165*, 725–737, doi:10.1144/0016-76492007/090.

Cruden, A. R. (1990), Flow and fabric development during the diapiric rise of magma, *J. Geol.*, *98*, 681–698, doi:10.1086/629433.

Culshaw, N., C. Beaumont, and R. A. Jamieson (2006), The orogenic superstructure-infrastructure concept: Revisited, quantified, and revived, *Geology*, *34*, 733–736, doi:10.1130/G22793.1.

de Sigoyer, J., V. Chavagnac, J. Blichert-Toft, I. M. Villa, B. Luais, S. Guillot, M. Cosca, and G. Mascle (2000), Dating the Indian continental subduction and collisional thickening in the northwest Himalaya: Multichronology of the Tso Morari eclogites, *Geology*, *28*, 487–490, doi:10.1130/0091-7613(2000)028<0487:DTICSA>2.3.CO;2.

de Sigoyer, J., S. Guillot, and P. Dick (2004), Exhumation of the ultrahigh-pressure Tso Morari unit in eastern Ladakh (NW Himalaya): A case study, *Tectonics*, *23*, TC3003, doi:10.1029/2002TC001492.

Dèzes, P. J., J.-C. Vannay, A. Steck, F. Bussy, and M. Cosca (1999), Synorogenic extension: Quantitative constraints on the age and displacement of the Zanskar shear zone (northwest Himalaya), *Geol. Soc. Am. Bull.*, *111*, 364–374, doi:10.1130/0016-7606(1999)111<0364:SEQCOT>2.3.CO;2.

Donaldson, D. G., A. A. G. Webb, C. A. Menold, A. R. C. Kylander-Clark, and B. R. Hacker (2013), Petrochronology of Himalayan ultrahigh-pressure eclogite, *Geology*, *41*, 835–838, doi:10.1130/G33699.1.

Epard, J.-L., and A. Steck (2008), Structural development of the Tso Morari ultra-high pressure nappe of the Ladakh Himalaya, *Tectonophysics*, *451*, 242–264, doi:10.1016/j.tecto.2007.11.050.

Fuchs, G. (1982), The geology of the Pin valley in Spiti, H.P., India, *Jahrb. Geol. Bundesanst.*, *124*, 325–359.

Gansser, A. (1964), *Geology of the Himalayas*, Wiley-Interscience, London.

Godin, L., R. L. Brown, S. Hanmer, and R. R. Parrish (1999), Back folds in the core of the Himalayan Orogen: An alternative interpretation, *Geology*, *27*(2), 151–154, doi:10.1130/0091-7613(1999)027<0151:BFITCO>2.3.CO;2.

Godin, L., R. L. Brown, R. R. Parrish, and K. V. Hodges (2001), Crustal thickening leading to exhumation of the Himalayan metamorphic core of central Nepal: Insight from U-Pb geochronology and ^{40}Ar/^{39}Ar thermochronology, *Tectonics*, *20*, 729–747, doi:10.1029/2000TC001204.

Godin, L., D. Grujic, R. Law, and M. P. Searle (2006), Crustal flow, extrusion, and exhumation in continental collision zones: An introduction, in *Channel Flows, Ductile Extrusion and Exhumation in Continental Collision Zones*, edited by R. D. Law, M. P. Searle, and L. Godin, *Geol. Soc. London, Spec. Publ.*, *268*, pp. 1–23.

Grasemann, B., H. Fritz, and J.-C. Vannay (1999), Quantitative kinematic flow analysis from the Main Central Thrust Zone (NW-Himalaya, India): Implications for a decelerating strain path and the extrusion of orogenic wedges, *J. Struct. Geol.*, *21*, 837–853, doi:10.1016/S0191-8141(99)00077-2.

Grujic, D., M. Casey, C. Davidson, L. S. Hollister, R. Kündig, T. Pavlis, and S. Schmid (1996), Ductile extrusion of the Higher Himalayan crystalline in Bhutan: Evidence from quartz microfabrics, *Tectonophysics*, *260*, 21–43, doi:10.1016/0040-1951(96)00074-1.

Grujic, D., L. S. Hollister, and R. R. Parrish (2002), Himalayan metamorphic sequence as an orogenic channel: Insight from Bhutan, *Earth Planet. Sci. Lett.*, *198*(1–2), 177–191, doi:10.1016/S0012-821X(02)00482-X.

Guillot, S., E. Garzanti, D. Baratoux, D. Marquer, G. Mahéo, and J. de Sigoyer (2003), Reconstructing the total shortening history of the NW Himalaya, *Geochem. Geophys. Geosyst.*, *4*(7), 1064, doi:10.1029/2002GC000484.

Harris, N., and J. Massey (1994), Decompression and anatexis of Himalayan metapelites, *Tectonics*, *13*, 1537–1546, doi:10.1029/94TC01611.

Harris, N., M. Ayres, and J. Massey (1995), Geochemistry of granitic melts produced during the incongruent melting of muscovite: Implications for the extraction of Himalayan leucogranite magmas, *J. Geophys. Res.*, *100*, 15,767–15,777, doi:10.1029/94JB02623.

Harrison, T. M., M. Grove, K. D. McKeegan, C. D. Coath, O. M. Lovera, and P. Le Fort (1999), Origin and episodic emplacement of the Manaslu intrusive complex, central Himalaya, *J. Petrol.*, *40*(1), 3–19, doi:10.1093/petroj/40.1.3.

Hauck, M. L., K. D. Nelson, L. D. Brown, W. J. Zhao, and A. R. Ross (1998), Crustal structure of the Himalayan orogen at similar to 90 degrees east longitude from project INDEPTH deep reflection profiles, *Tectonics*, *17*, 481–500, doi:10.1029/98TC01314.

Hintersberger, E., R. C. Thiede, M. R. Strecker, and B. R. Hacker (2010), East-west extension in the NW Indian Himalaya, *Geol. Soc. Am. Bull.*, *122*(9–10), 1499–1515, doi:10.1130/B26589.1.

Hintersberger, E., R. C. Thiede, and M. R. Strecker (2011), The role of extension during brittle deformation within the NW Indian Himalaya, *Tectonics*, *30*, TC3012, doi:10.1029/2010TC002822.

Hodges, K. V. (2000), Tectonics of the Himalaya and southern Tibet from two perspectives, *Geol. Soc. Am. Bull.*, *112*(3), 324–350, doi:10.1130/0016-7606(2000)112<324:TOTHAS>2.0.CO;2.

Hodges, K. V., R. R. Parrish, and M. P. Searle (1996), Tectonic evolution of the central Annapurna Range, Nepalese Himalayas, *Tectonics*, *15*, 1264–1291, doi:10.1029/96TC01791.

Hodges, K. V., J. M. Hurtado, and K. X. Whipple (2001), Southward extrusion of Tibetan crust and its effect on Himalayan tectonics, *Tectonics*, *20*, 799–809, doi:10.1029/2001TC001281.

Holdaway, M. J. (2000), Application of new experimental and garnet Margules data to the garnet-biotite geothermometer, *Am. Mineral.*, *85*, 881–892, doi:10.2138/am-2000-0701.

Holland, T. J. B., and R. Powell (1998), An internally consistent thermodynamic data set for phases of petrological interest, *J. Metamorph. Geol.*, *16*(3), 309–343, doi:10.1111/j.1525-1314.1998.00140.x.

Horton, F., J. Lee, B. R. Hacker, M. Bowman-Kamaha'o, and M. Cosca (2014), Himalayan gneiss dome formation in the middle crust and exhumation by normal faulting: New geochronology of Gianbul dome, northwestern India, *Geol. Soc. Am. Bull.*, *127*(1–2), 162–180, doi:10.1130/B31005.1.

Inger, S., and N. B. W. Harris (1992), Tectonothermal evolution of the high Himalayan crystalline sequence, Langtang Valley, northern Nepal, *J. Metamorph. Geol.*, *10*(3), 439–452, doi:10.1111/j.1525-1314.1992.tb00095.x.

Jamieson, R. A., and C. Beaumont (2013), On the origin of orogens, *Geol. Soc. Am. Bull.*, *125*, 1671–1702, doi:10.1130/B30855.1.

Jessup, M. J., J. M. Cottle, M. P. Searle, R. D. Law, R. J. Tracy, T. L. Newell, and D. J. Waters (2008), *P-T-t-D* paths of the Everest Series schist, Nepal, *J. Metamorph. Geol.*, *26*, 717–739, doi:10.1111/j.1525-1314.2008.00784.x.

Kellett, D. A., and D. Grujic (2012), New insight into the South Tibetan detachment system: Not a single progressive deformation, *Tectonics*, *31*, TC2007, doi:10.1029/2011TC002957.

Kellett, D. A., D. Grujic, C. Warren, J. M. Cottle, R. A. Jamieson, and T. Tenzin (2010), Metamorphic history of a syn-convergent orogen parallel detachment: The South Tibetan detachment system, Bhutan Himalaya, *J. Metamorph. Geol.*, *28*, 785–808, doi:10.1111/j.1525-1314.2010.00893.x.

King, J., N. Harris, T. Argles, R. Parrish, B. Charlier, S. Sherlock, and H. F. Zhang (2007), First field evidence of southward ductile flow of Asian crust beneath southern Tibet, *Geology*, *35*(8), 727–730, doi:10.1130/G23630A.1.

Kohn, M. J., and F. Spear (2000), Retrograde net transfer reaction insurance for pressure-temperature estimates, *Geology*, *28*, 1127–1130, doi:10.1130/0091-7613(2000)28<1127:RNTRIF>2.0.CO;2.

Langille, J., J. Lee, B. Hacker, and G. Seward (2010), Middle crustal ductile deformation patterns in southern Tibet: Insights from vorticity studies in Mabja Dome, *J. Struct. Geol.*, *32*, 70–85, doi:10.1016/j.jsg.2009.08.009.

Langille, J. M., M. J. Jessup, J. M. Cottle, G. Lederer, and T. Ahmad (2012), Timing of metamorphism, melting and exhumation of the Leo Pargil dome, northwest India, *J. Metamorph. Geol.*, *30*, 769–791, doi:10.1111/j.1525-1314.2012.00998.x.

Langille, J. M., M. J. Jessup, J. Cottle, and T. Ahmad (2014), Kinematic and thermal studies of the Leo Pargil Dome: Implications for syncon-vergent extension in the NW Indian Himalaya, *Tectonics*, *33*, 1766–1786, doi:10.1002/2014TC003593.

Larson, K. P., L. Godin, W. J. Davis, and D. W. Davis (2010), Out-of-sequence deformation and expansion of the Himalayan orogenic wedge: Insight from the Changgo culmination, south central Tibet, *Tectonics*, *29*, TC4013, doi:10.1029/2008TC002393.

Law, R. D., D. W. Stahr III, M. K. Francsis, K. T. Ashley, B. Grasemann, and T. Ahmad (2013), Deformation temperatures and flow vorticities near the base of the Greater Himalayan Series, Sutlej Valley and Shimla Klippe, NW India, *J. Struct. Geol.*, *54*, 21–53, doi:10.1016/j.jsg.2013.05.009.

Lederer, G., J. Cottle, M. Jessup, J. Langille, and T. Ahmad (2013), Time-scales of partial melting in the Himalayan middle crust: Insight from the Leo Pargil dome, northwest India, *Contrib. Mineral. Petrol.*, *166*, 1415–1441, doi:10.1007/s00410-013-0935-9.

Lee, J., and M. J. Whitehouse (2007), Onset of mid-crustal extensional flow in southern Tibet: Evidence from U/Pb zircon ages, *Geology*, *35*, 45–48, doi:10.1130/G22842A.1.

Lee, J., B. R. Hacker, W. S. Dinklage, Y. Wang, P. Gans, A. Calvert, J. Wan, W. Chen, A. E. Blythe, and W. McClelland (2000), Evolution of the Kangmar Dome, southern Tibet: Structural, petrologic, and thermochronologic constraints, *Tectonics*, *19*, 872–895, doi:10.1029/1999TC001147.

Lee, J., B. R. Hacker, and Y. Wang (2004), Evolution of North Himalayan gneiss domes: Structural and metamorphic studies in Mabja Dome, southern Tibet, *J. Struct. Geol.*, *26*, 2297–2316, doi:10.1016/j.jsg.2004.02.013.

Lee, J., W. McClelland, Y. Wang, A. Blythe, and M. McWilliams (2006), Oligocene-Miocene mid-crustal flow in southern Tibet: Geochronology of Mabja Dome, in *Channel Flow, Ductile Extrusion and Exhumation in Continental Collision Zones*, edited by R. D. Law, M. P. Searle, and L. Godin, *Geol. Soc. London, Spec. Publ.*, *268*, pp. 445–469.

Leech, M. L. (2008), Does the Karakoram fault interrupt mid-crustal channel flow in the western Himalaya?, *Earth Planet. Sci. Lett.*, *276*, 314–322, doi:10.1016/j.epsl.2008.10.006.

Leech, M. L., S. Singh, A. K. Jain, S. L. Klemperer, and R. M. Manickavasagam (2005), The onset of India-Asia continental collision: Early, steep subduction required by the timing of UHP metamorphism in the western Himalaya, *Earth Planet. Sci. Lett.*, *234*(1–2), 83–97, doi:10.1016/j.epsl.2005.02.038.

Leech, M. L., S. Singh, and A. K. Jain (2007), Continuous metamorphic zircon growth and interpretation of U-Pb SHRIMP dating: An example from the Western Himalaya, *Int. Geol. Rev.*, *49*(4), 313–328, doi:10.2747/0020-6814.49.4.313.

Leger, R. M., A. A. G. Webb, D. J. Henry, J. A. Craig, and P. Dubey (2013), Metamorphic field gradients across the Himachal Himalaya, northwest India: Implications for the emplacement of the Himalayan crystalline core, *Tectonics*, *32*, 540–557, doi:10.1002/tect.20020.

Miller, C., M. Thoni, W. Frank, B. Grasemann, U. Klotzli, P. Guntli, and E. Draganits (2001), The early Palaeozoic magmatic event in the Northwest Himalaya, India: Source, tectonic setting and age of emplacement, *Geol. Mag.*, *138*(3), 237–251, doi:10.1017/S0016756801005283.

Molnar, P., and J. M. Stock (2009), Slowing of India's convergence with Eurasia since 20 Ma and its implications for Tibetan mantle dynamics, *Tectonics*, *28*, TC3001, doi:10.1029/2008TC002271.

Nabelek, P. I., A. G. Whittington, and A. M. Hofmeister (2010), Strain heating as a mechanism for partial melting and ultrahigh temperature metamorphism in convergent orogens: Implications of temperature-dependent thermal diffusivity and rheology, *J. Geophys. Res.*, *115*, B12417, doi:10.1029/2010JB007727.

Nelson, K. D., et al. (1996), Partially molten middle crust beneath southern Tibet: Synthesis of project INDEPTH results, *Science*, *274*, 1684–1688, doi:10.1126/science.274.5293.1684.

Neumayer, J., G. Wiesmayr, C. Janda, B. Grasemann, and E. Draganits (2004), Eohimalayan fold and thrust belt in the NW-Himalaya (Lingti-Pin Valleys): Shortening and the depth to detachment calculation, *Austrian J. Earth Sci.*, *95/96*, 28–36.

Passchier, C. W., and R. A. J. Trouw (2005), *Microtectonics*, 2nd ed., Springer, Berlin.

Patiño Douce, A. E., and N. B. W. Harris (1998), Experimental constraints on Himalayan anatexis, *J. Petrol.*, *39*(4), 689–710, doi:10.1093/petroj/39.4.689.

Pattison, D. R. M., F. S. Spear, and J. T. Cheney (1999), Polymetamorphic origin of muscovite+cordierite+staurolite+biotite assemblages: Implications for the metapelitic petrogenetic grid and for *P–T* paths, *J. Metamorph. Geol.*, *17*, 685–703, doi:10.1046/j.1525-1314.1999.00225.x.

Powell, R., and T. Holland (1994), Optimal geothermometry and geobarometry, *Am. Mineral.*, *79*(1–2), 120–133.

Pownceby, M. I., V. J. Wall, and H. S. Oneill (1987), Fe-Mn partitioning between garnet and ilmenite—Experimental calibration and applica-tions, *Contrib. Mineral. Petrol.*, *97*(1), 116–126, doi:10.1007/BF00375219.

Pownceby, M. I., V. J. Wall, and H. S. C. Oneill (1991), An experimental-study of the effect of Ca upon garnet-ilmenite Fe-Mn exchange equilibria, *Am. Mineral.*, *76*(9–10), 1580–1588.

Quigley, M. C., L. Yu, X. Liu, C. J. L. Wilson, M. Sandiford, and D. Phillips (2006), [40]Ar/[39]Ar thermochronology of the Kampa Dome, southern Tibet: Implications for tectonic evolution of the North Himalayan gneiss domes, *Tectonophysics*, *421*, 269–297, doi:10.1016/j.tecto.2006.05.002.

Quigley, M. C., L. Yu, C. Gregory, A. Corvino, M. Sandiford, C. J. L. Wilson, and X. Liu (2008), U-Pb SHRIMP zircon geochronology and *T-t-d* history of the Kampa Dome, southern Tibet, *Tectonophysics*, *446*, 97–113, doi:10.1016/j.tecto.2007.11.004.

Ratschbacher, L., W. Frisch, G. Liu, and C. Chen (1994), Distributed deformation in southern and western Tibet during and after the India-Asia collision, *J. Geophys. Res.*, *99*, 19,917–19,945, doi:10.1029/94JB00932.

Robyr, M., J.-C. Vannay, J. L. Epard, and A. Steck (2002), Thrusting extension and doming during polyphase tectometamorphic evolution of the High Himalayan Crystalline Zone in NW India, *J. Asian Earth Sci.*, *21*, 221–239, doi:10.1016/S1367-9120(02)00039-1.

Robyr, M., B. R. Hacker, and J. M. Mattinson (2006), Doming in compressional orogenic settings: New geochronological constraints from the NW Himalaya, *Tectonics*, *25*, TC2007, doi:10.1029/2004TC001774.

Searle, M. P. (1986), Structural evolution and sequence of thrusting in the High Himalayan, Tibetan-Tethys and Indus suture zones of Zanskar and Ladakh, Western Himalaya, *J. Struct. Geol.*, *8*(8), 923–936, doi:10.1016/0191-8141(86)90037-4.

Searle, M. P. (2010), Low-angle normal faults in the compressional Himalayan orogen: Evidence from the Annapurna-Dhaulagiri Himalaya, Nepal, *Geosphere*, *6*(4), 296–315, doi:10.1130/GES00549.1.

Searle, M. P., and L. Godin (2003), The South Tibetan detachment and the Manaslu Leucogranite; a structural reinterpretation and restoration of the Annapurna-Manaslu Himalaya, Nepal, *J. Geol.*, *111*(5), 505–523, doi:10.1086/376763.

Searle, M. P., et al. (1987), The closing of Tethys and the tectonics of the Himalaya, *Geol. Soc. Am. Bull.*, *98*(6), 678–701, doi:10.1130/0016-7606(1987)98<678:TCOTAT>2.0.CO;2.

Searle, M. P., K. T. Pickering, and D. J. W. Cooper (1990), Restoration and evolution of the intermontane Indus Molasse Basin, Ladakh Himalaya, India, *Tectonophysics*, *174*(3–4), 301–314, doi:10.1016/0040-1951(90)90327-5.

Searle, M. P., R. I. Corfield, B. Stephenson, and J. McCarron (1997), Structure of the north Indian continental margin in the Ladakh-Zanskar Himalayas: Implications for the timing of obduction of the Spontang ophiolite, India-Asia collision and deformation events in the Himalaya, *Geol. Mag.*, *134*, 297–316.

Searle, M. P., R. L. Simpson, R. D. Law, R. R. Parrish, and D. J. Waters (2003), The structural geometry, metamorphic and magmatic evolution of the Everest massif, High Himalaya of Nepal-South Tibet, *J. Geol. Soc. London*, *160*, 345–366, doi:10.1144/0016-764902-126.

Steck, A. (2003), Geology of the NW Indian Himalaya, *Eclogae Geol. Helv.*, *96*, 147–196, doi:10.1007/s00015-003-1091-4.

Steck, A., L. Spring, J.-C. Vannay, H. Masson, E. Stutz, H. Bucher, R. Marchant, and J. C. Tieche (1993), Geological transect across the northwestern Himalaya in eastern Ladakh and Lahul (a model for the continental collision of India and Asia), *Eclogae Geol. Helv.*, *86*(1), 219–263, doi:10.5169/seals-167241.

St-Onge, M. R., N. Rayner, R. M. Palin, M. P. Searle, and D. J. Waters (2013), Integrated pressure-temperature-time constraints for the Tso Morari dome (northwest India): Implications for the burial and exhumation path of UHP units in the western Himalaya, *J. Metamorph. Geol.*, *31*(5), 469–504, doi:10.1111/jmg.12030.

Stübner, K., D. Grujic, R. R. Parrish, N. M. W. Roberts, A. Kronz, J. Wooden, and T. Ahmad (2014), Monazite geochronology unravels the timing of crustal thickening in NW Himalaya, *Lithos*, *210–211*, 111–128, doi:10.1016/j.lithos.2014.09.024.

Thiede, R. C., J. R. Arrowsmith, B. Bookhagen, M. McWilliams, E. R. Sobel, and M. R. Strecker (2006), Dome formation and extension in the Tethyan Himalaya, Leo Pargil, northwest India, *Geol. Soc. Am. Bull.*, *118*, 635–650, doi:10.1130/B25872.1.

Thiede, R. C., T. A. Ehlers, B. Bookhagen, and M. R. Strecker (2009), Erosional variability along the northwest Himalaya, *J. Geophys. Res.*, *114*, F01015, doi:10.1029/2008JF001010.

Vance, D., and N. Harris (1999), Timing of prograde metamorphism in the Zanskar Himalaya, *Geology*, *27*(5), 395–398, doi:10.1130/0091-7613(1999)027<0395:TOPMIT>2.3.CO;2.

Vance, D., and E. Mahar (1998), Pressure-temperature paths from *P-T* pseudosections and zoned garnets: Potential, limitations and examples from the Zanskar Himalaya, NW India, *Contrib. Mineral. Petrol.*, *132*, 225–245, doi:10.1007/s004100050419.

Vannay, J.-C., and B. Grasemann (1998), Inverted metamorphism in the High Himalaya of Himachal Pradesh (NW India): Phase equilibria versus thermobarometry, *Schweiz. Mineral. Petrogr. Mitt.*, *78*, 107–132.

Vannay, J.-C., and B. Grasemann (2001), Himalayan inverted metamorphism and syn-convergence extension as a consequence of a general shear extrusion, *Geol. Mag.*, *138*, 253–276, doi:10.1017/S0016756801005313.

Vannay, J.-C., Z. D. Sharp, and B. Grasemann (1999), Himalayan inverted metamorphism constrained by oxygen isotope thermometry, *Contrib. Mineral. Petrol.*, *137*(1–2), 90–101.

Vannay, J.-C., B. Grasemann, M. Rahn, W. Frank, A. Carter, V. Baudraz, and M. Cosca (2004), Miocene to Holocene exhumation of metamorphic crustal wedges in the NW Himalaya: Evidence for tectonic extrusion coupled to fluvial erosion, *Tectonics*, *23*, TC1014, doi:10.1029/2002TC001429.

Webb, A. A. G., A. Yin, T. M. Harrison, J. Célérier, and W. P. Burgess (2007), The leading edge of the Greater Himalayan Crystallines revealed in the NW Indian Himalaya: Implications for the evolution of the Himalayan orogen, *Geology*, *35*(10), 955–958, doi:10.1130/G23931A.1.

Webb, A. A. G., A. Yin, T. M. Harrison, J. Célérier, G. E. Gehrels, C. E. Manning, and M. Grove (2011), Cenozoic tectonic history of the Himachal Himalaya (northwestern India) and its constraints on the formation mechanism of the Himalayan orogen, *Geosphere*, *7*, 1013–1061, doi:10.1130/GES00627.1.

Weinberg, R. F., and J. W. Dunlap (2000), Growth and deformation of the Ladakh Batholith, northwest Himalayas: Implications for timing of continental collision and origin of calc-alkaline batholiths, *J. Geol.*, *108*, 303–320, doi:10.1086/314405.

Weinberg, R. F., and P. Hasalová (2015), Water-fluxed melting of the continental crust: A review, *Lithos*, *212–215*, 158–188, doi:10.1016/j.lithos.2014.08.021.

White, L. T., and G. S. Lister (2012), The collision of India with Asia, *J. Geodyn.*, *56-57*, 7–17, doi:10.1016/j.jog.2011.06.006.

Wiesmayr, G., and B. Grasemann (2002), Eohimalayan fold and thrust belt: Implications for the geodynamic evolution of the NW-Himalaya (India), *Tectonics*, *21*(6), 1058, doi:10.1029/2002TC001363.

Yin, A. (2006), Cenozoic tectonic evolution of the Himalayan orogen as constrained by along-strike variation of structural geometry, exhumation history, and foreland sedimentation, *Earth Sci. Rev.*, *76*, 1–131, doi:10.1016/j.earscirev.2005.05.004.

Yin, A., and T. Harrison (2000), Geological evolution of the Himalayan-Tibetan orogen, *Annu. Rev. Earth Planet. Sci.*, *28*, 211–280, doi:10.1146/annurev.earth.28.1.211.

Zhang, J., L. Ding, D. Zhong, and Y. Zhou (2000), Orogen-parallel extension in Himalaya: Is it the indicator of collapse or the product in process of compressive uplift?, *Chin. Sci. Bull.*, *45*(2), 114–120.

Zhuang, G., Y. Najman, S. Guillot, M. Roddaz, P. Antoine, G. Métais, A. Carter, L. Marivaux, and S. Solangi (2015), Constraints on the collision and the pre-collision tectonic configuration between India and Asia from detrital geochronology, thermochronology, and geochemistry studies in the lower Indus basin, Pakistan, *Earth Planet. Sci. Lett.*, *432*, 363–373, doi:10.1016/j.epsl.2015.10.026.